2021

Monitoring of Overhead Polymer Core Composite Conductors Under Excessive Mechanical Loads Using Fiber Bragg Grating Sensors

Daniel H. Waters

Monitoring of Overhead Polymer Core Composite Conductors under Excessive Mechanical Loads using Fiber Bragg Grating Sensors

---

A Dissertation

Presented to

the Faculty of the Daniel Felix Ritchie School of Engineering and Computer Science

University of Denver

In Partial Fulfillment

of the Requirements for the Degree

Doctor of Philosophy

---

by

Daniel H. Waters

November 2021

Advisor: Dr. Maciej Kumosa

Author: Daniel H. Waters
Title: Monitoring of Overhead Polymer Core Composite Conductors under Excessive Mechanical Loads using Fiber Bragg Grating Sensors
Advisor: Dr. Maciej Kumosa
Degree Date: November 2021

Abstract

This combined experimental and numerical study addresses mechanical effects associated with static and dynamic loading of novel High Temperature Low Sag (HTLS) transmission line polymer core composite conductors. The developed methodology was successfully applied to ACCC® to explain the complex failure mechanisms associated with combined bending and tension loading. Furthermore, the use of Fiber Bragg Grating (FBG) sensors was investigated for the first time to monitor the ACCC® design during installation and in-service.

Transverse low-velocity impacts to the ACCC® conductor having either free or constrained end conditions and large axial tensile loads were performed. It was identified that the most damaging condition under impact is when the conductor had free ends and was thus subjected to severe bending. The experimental work performed using an original approach was supported by non-linear static and dynamic finite element analyses.

For the multiaxial case of rods subjected to bending and axial tension, the axial stresses were predicted analytically and numerically with the likely failure initiating locations identified based on the theoretical composite compressive strengths. The initiating damage mechanisms change from compressive to tensile modes as axial tension increases. It has been shown for the first time that the natural presence of fiber

misalignment must be considered in the failure analysis of hybrid composite rods as it can significantly reduce bending strength and influence the location of damage initiation.

It has been demonstrated that FBG sensing is a viable technique for in-service monitoring of ACCC® conductors subjected to a variety of static and impact situations. Under static and low energy/velocity conditions, surface mounted sensors can accurately measure strains both on the bare rods and inside the conductors. The tests on the full-scale conductors under low energy impact also showed that the sensors can identify the location and magnitude of impact with a high degree of sensitivity. These results, combined with the intrinsic properties of optical sensors and fibers, indicate the FBG sensors could be especially useful in the monitoring of low and high energy impact events in-service. Finally, an evaluation of using of embedded FBG sensors inside the hybrid composite core of ACCC® is presented.

Acknowledgements

Finally, at the culmination of my graduate studies, there are many people I am obliged to thank. By many days, and countless hours, their assistance gave rise to this research and dissertation, and for that, they will ever have my deepest gratitude. This work would not have been possible without the support of the NSF Center for Novel High Voltage/Temperature Materials and Structures. In particular, I am most grateful to the Western Area Power Administration (WAPA), the Bonneville Power Administration (BPA), the Tri-State Generation and Transmission Association and CTC Global for providing materials, expertise, and guidance throughout the entire study. Many thanks to my advisor, Dr. Maciej Kumosa, for his overall support, and for continuously believing I could aspire to this level of science and academic excellence. I must also thank Dr. Joe Hoffman, Dr. Euripides Solis-Ramos, and Dr. Paul Predecki for their productive insightful discourse and their assistance with experimental work. I relied on their friendship, experience and hard work many times. I also express my appreciation towards Mr. Jon Buckley, for his friendship, teaching, valuable insight, and extensive knowledge of manufacturing, without whom I would have not been able to design and fabricate the unique fixtures so critical for my research.

List of Figures

List of Tables

1 Introduction

1.1 Growing demand for power

Modern society has significant dependence on electrical power, and with a constantly increasing demand, significant strain is placed on the current electrical grid. Utilities are faced with the challenge to meet these requirements by upgrading or replacing existing infrastructure. In the United States, the grid in Figure 1-1 is a network of overhead transmission lines, substations, and power generation plants combined to provide power to end users (Figure 1-2). This dissertation focuses on the bare high voltage overhead conductors used in the transmission phase between the generation sites and substations.

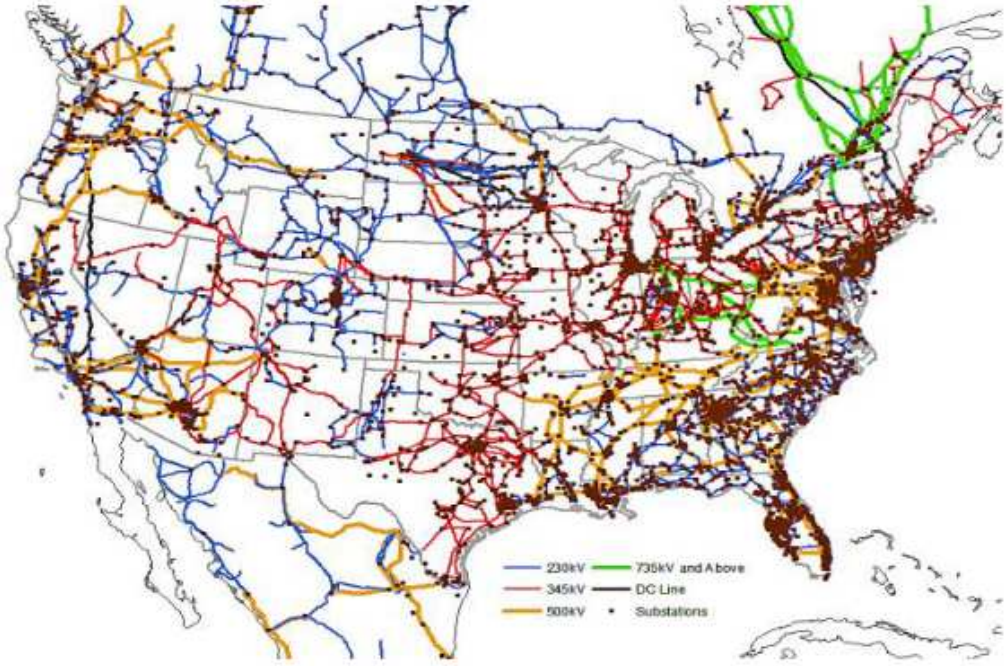

Figure 1-1: US Electrical Transmission Grid [1].

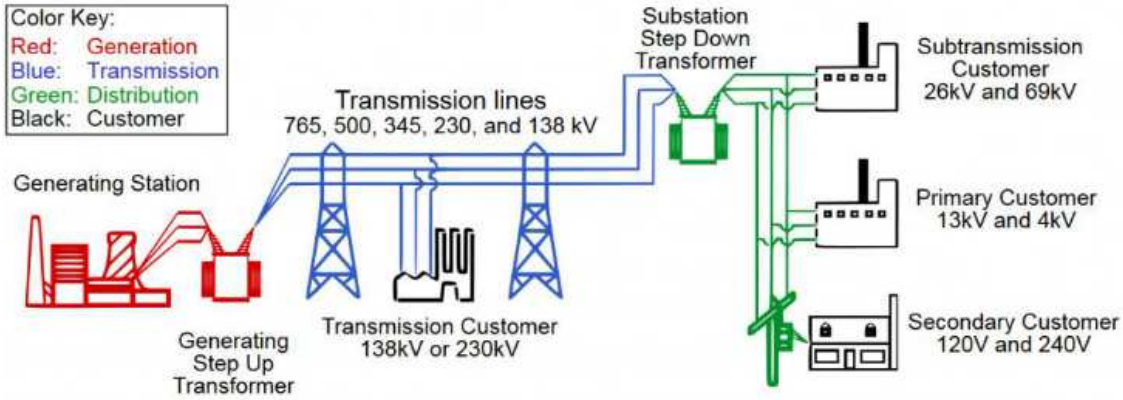

Figure 1-2:Power Generation and Transmission Schematic[2].

1.2 Existing conductor designs

Currently, four major designs of bare overhead conductors are used as transmission lines (Figure 1-3). Conventional designs of Aluminum Conductor Steel Reinforced (ACSR) (standard in the industry since the early 1900's [3]) and higher strength

Aluminum Conductor Steel Supported (ACSS) consist of aluminum stranding for electrical conductivity wound around steel strands for mechanical strength. The thermal mechanical behavior of these materials, however, limits the amount of power conventional designs can transmit. As the transmission line temperature increases with increasing electrical current, thermal expansion of the conductor can cause line-sag to exceed safe limits and lead to potential short-circuits with trees or surrounding structures. In August of 2003, sagging lines caused a blackout across much of Ontario and the eastern United States [4]. One method considered by the power transmission industry to keep up with the ever-increasing demand, is to re-conductor existing rights of way with a new class of High-Temperature Low-Sag (HTLS) transmission lines [5]. According to Clairmont [6], the cost of HTLS conductors are 2-12 times more expensive than that of conventional conductors, but the same diameter and weight HTLS conductor can carry twice the current without the need to replace existing towers. Two such HTLS conductors are ACCC® and Aluminum Conductor Composite Reinforced (ACCR), both of which utilize composite load-bearing components that are lighter, stronger, and allow increased operating temperatures over ACSR without losing strength to annealing or exceeding minimum sag clearances.

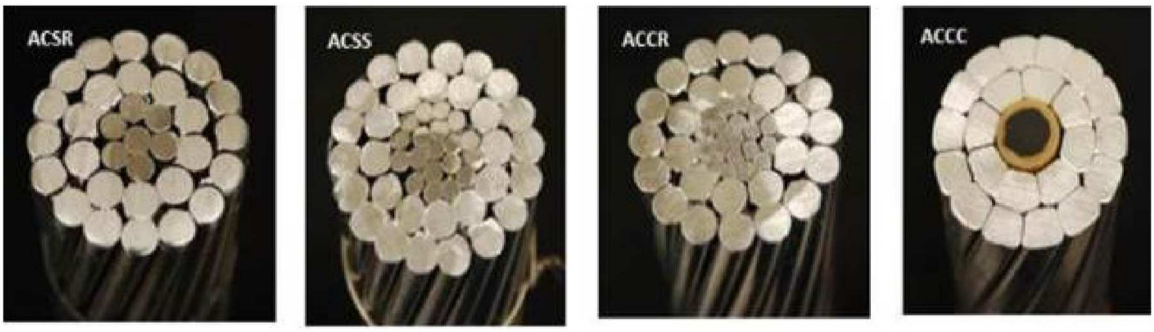

Figure 1-3: HV overhead conductor designs currently in use [7].

1.3 ACCC®

ACCC® , shown in Figure 1-4, is manufactured by CTC Global and has a hybrid Polymer Matrix Composite (PMC) core consisting of high strength carbon fibers with a high temperature epoxy resin surrounded by a galvanic corrosion barrier of ECR-glass fibers with the same resin [8]. The conducting strands consist of 1350-O aluminum with a trapezoidal cross-section. The Drake size ACCC® core addressed in this document consists of a nominal diameter of 6.74 mm of unidirectional Carbon Fiber/Epoxy surrounded by an additional layer of unidirectional ECR-Glass/Epoxy to achieve an overall outer diameter of 9.53 mm. This composite core has a rated tensile strength of 2158 MPa with typical installation loads up to 22.2 kN and service loads of 40 kN [9].

Despite the potential benefits, some utilities are reluctant to use these novel HTLS conductors, owing to a combination of unfamiliarity in material behavior of the composite under long term service conditions and a poor knowledge of the reliability of the composite design [4]. Although the majority of installations have been successful, several incidents have occurred where ACCC® conductors failed during or shortly after installation.

Figure 1-4: Components of ACCC® conductor [10].

1.4 Publications related to this work

With collaborative efforts at the National Science Foundation Center for Novel High Voltage/Temperature Materials and Structures (HVT Center), the work presented in this dissertation has resulted in numerous technical reports, and publications.

Publications:

- D. H. Waters, "Low-Velocity Impact to High-Temperature Low-Sag Overhead Conductors," Masters Thesis, University of Denver, 2016.
- D. H. Waters, J. Hoffman, E. Hakansson, and M. Kumosa, "Low-Velocity Impact to Transmission Line Conductors," Int. J. Impact Eng., vol. 106, pp. 64–72, 2017.

- J. Hoffman, D. H. Waters, S. Khadka, and M. S. Kumosa, “Shape Sensing of Polymer Core Composite Electrical Transmission Lines Using FBG Sensors,” IEEE Trans. Instrum. Meas., vol. PP, pp. 1–9, 2019.
- D. H. Waters, J. Hoffman, and M. Kumosa, “Monitoring of Overhead Transmission Conductors Subjected to Static and Impact Loads Using Fiber Bragg Grating Sensors,” IEEE Trans. Instrum. Meas., vol. 68, no. 2, pp. 595–605, 2019.
- D. Waters, J. Hoffman, and M. Kumosa, “Effect of Fiber Misalignment on Bending Strength of Pultruded Hybrid Polymer Matrix Composite Rods Subjected to Bending and Tension,” Compos. Part A Appl. Sci. Manuf., vol. 143, no. October 2020, p. 106287, Apr. 2021.

Annual Reports made to the Industry-University Cooperative Research Centers (IUCRC) Center for Novel High Voltage/Temperature Materials and Structures:

- **D.H. Waters**. Impact Damage to High Voltage Conductors. November 17-18, 2014. University of Illinois at Urbana-Champaign.
- **D.H. Waters**. Impact Damage to High Voltage Conductors. May 19-20, 2015. Michigan Technological University.
- **D.H. Waters**. Low Velocity Impact Damage to Current and Novel HV Conductors. May 16-18, 2016. University of Illinois at Urbana-Champaign.
- J. Hoffman, **D.H. Waters**, et al. HVT Monitoring using Fiber Bragg Gratings and other Techniques. May 16-17, 2017. Hyatt Regency Denver Tech Center.

- J. Hoffman, **D.H. Waters**. Health Monitoring of HVT Structures using FBGs. May 14-16, 2018. University of Illinois at Urbana-Champaign.

The response to low-velocity impacts during transportation, installation or in service, of ACCC®, had not yet been addressed in literature prior to this work. Chapter 2 contains information related to the Master's thesis but was published during the PhD work. It is included in this dissertation due to its relevance to all the remaining work.

2 Low-velocity impact to transmission line conductors

2.1 Introduction

Extensive research has been conducted on the impact resistance of fiber-reinforced PMC laminates, for example see [11]–[16], where damage from low-velocity and high-velocity projectiles was investigated given various properties of fibers and matrices. The results, however, are limited to flat laminate plates typically used in aerospace and ballistic protection applications. No research has been found pertaining to any low-velocity impacts to stranded traditional conductors, HTLS conductors, or more specifically to ACCC®.

Limited work has been conducted to help characterize the mechanical properties of ACCC® under static and dynamic loading conditions [8], [17]–[21]. Research specific to the bending strength of the PMC rod was conducted by Burks, et al. to determine the minimum static bend radius to initiate damage at the Glass/Carbon interface or at any point within the composite rod [17]. Burks also quantified the residual tensile strength of the hybrid composite rod after excessive static bending [18], a result that can only be applied to static loading conditions. It has also been shown by Burks, that under severe bending beyond the critical bend radius, the ACCC® rod can rapidly collapse and the failure is initiated by the kinking of carbon fibers on the compressive side of the rods [17], [18].

The absence of available research on the mechanical response of transmission conductors, including next generation conductors based on PMCs, subjected to low-velocity impact was the driving force behind the research performed in this chapter. The results obtained allow for a much better understanding of both the damage mechanisms in all types of polymer core composite conductors and the conditions that can be most damaging and should be avoided during installation and in service.

2.2 Experimental methods

2.2.1 Tested conductors and sample preparation

The ACCC® conductor evaluated in this research (Figure 1-4) was received from the Western Area Power Administration (WAPA). ACCC® consists of the hybrid epoxy PMC core surrounded by an inner layer of 8 and an outer layer of 14 helically wound trapezoidal cross-section 1350-O aluminum strands. The overall outer diameter was $28.2mm$. The diameter of the composite rod was 9.3 mm. More properties of the materials of the conductor are presented and discussed in subsequent sections.

2.2.2 Impact fixture design

A specialized impact test fixture was designed and constructed in this research to perform impact tests on the conductors (Figure 2-1). The tests used a weighted pendulum and the energy transfer was measured by angular position similar to a Charpy-Izod impact tester. ACCC® samples of $l = 1.10\ m$ in length were held in custom-built clamps designed to grip the conductors through the outer aluminum stranding and transfer the loading to the core, as seen in Figure 2-2.

Tension in the samples was measured by assuming a frictionless first-class lever having a mechanical advantage of $ma = 6.4$. A ratcheting chain puller and a Dillion

Mechanical AP Dynamometer were used to increase, hold, and measure the tension on the input side of the tensioning lever arms. The measured input tension was then multiplied by the mechanical advantage to calculate the sample tension. Once the desired tension was reached, the dynamometer and chain-hoist were replaced by a turnbuckle-tensioning device to fix the displacement of lever input arms. The calibration of the tensioning method was verified with strain gauges.

Angular position of the pendulum arm was measured using an optical rotary encoder attached to the pendulum axle. The angle encoder had a sensitivity of $\pi/1200\ Rad/pulse$, or $2400\ pulse/rev$. Energies of the rotating pendulum were calculated using the equation of kinetic energy in a rotating system, $KE = 0.5I\omega^2$, where ω is the instantaneous angular velocity of the pendulum and I is the moment of inertia of the pendulum. I was experimentally determined using the equation for the moment of inertia about a fixed pivot, $I_{ZZ} = Wr(\tau/2\pi)^2$. The period, τ, weight, W, and radius to the center of mass, r, were measured for the entire assembly of the pendulum, four lead bricks, cylinder impactor, and ratchet straps.

The period, τ, of the free swinging pendulum was $2.325\ s$. The total mass of the assembled pendulum, W, consisting of four lead bricks, cylinder impactor, and ratchet straps was $56.9\ kg$. The radius to the center of mass, r, was $1.22\ m$. The resulting mass moment of inertia, I_{zz} for the instrumented pendulum was determined to be $93.2\ Nms^2$.

In the first part of the mechanical testing, static bending experiments were performed on the conductor subjected to both transverse static bending and axial tension. This was done to verify the accuracy of the numerical modeling under static conditions. Conductor

deflections were measured for a static transverse loading of 1.00 kN imparted by a cylindrical steel tool of diameter 41.3mm and initial axial tensions between 11.47 kN and 43.00 kN. 1.00 kN was chosen to provide a different boundary condition while remaining within the design capacity of the testing apparatus.

Subsequently, low velocity impact tests were conducted for boundary conditions of fixed displacement ends at initial tensions of 1.15 kN, 4.59 kN, 11.5 kN, 20.1 kN and 29.2 kN as well as a 3-point impact condition where the conductor was supported across 25.4mm square support posts separated by 0.46 m. Initial height for release was set at approximately $\pi/4\ Rad$ above the point of contact. A cylindrical steel impacting tool of diameter 41.3mm attached to the end of the pendulum struck transverse to the axial direction of the conductor for all tests. Time history of the angular position of the pendulum was recorded for each test and analyzed with MATLAB® to calculate angular velocity and kinetic energy stored in the pendulum. Seven samples were tested in the 3-point impact condition of no axial constraints. For the fixed-displacement boundary conditions two samples were tested at each of the five initial tensions.

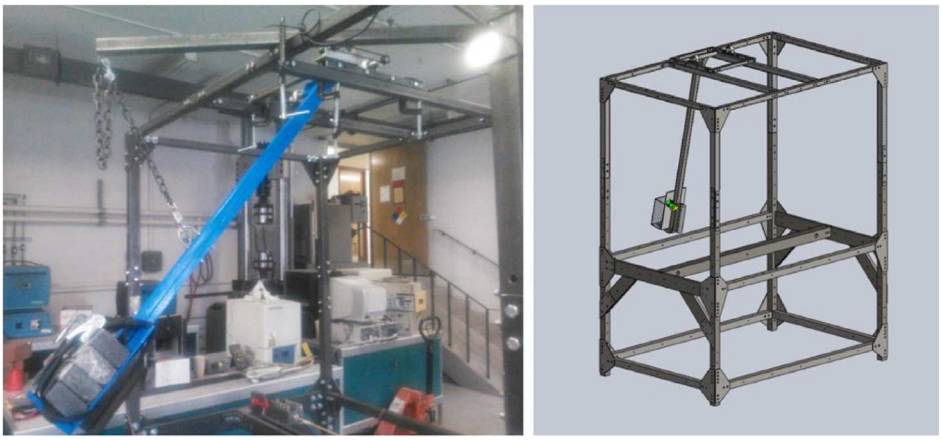

Figure 2-1: Pendulum impacting design.

Figure 2-2: Conductor clamp and cable tensioning.

2.3 Numerical methods

2.3.1 Simplified conductor model

Numerical modeling was performed to help understand the energy transfer into the ACCC® conductor when exposed to low-velocity impact. Quantities not measured in the experiment, such as friction, plastic strain, and elastic strain, may depend on the boundary conditions and can identify how the conductor is storing or dissipating energy. The structural models of the conductor were simplified but representative in their geometry and boundary condition (Figure 2-3 and Figure 2-4) to identify possible trends and contribute to the understanding of the actual experiments. This type of simplification could be very useful when modeling actual full length in service conductors spanning thousands of meters. Obviously, modeling full scale locally damaged conductors in service would be computationally not feasible.

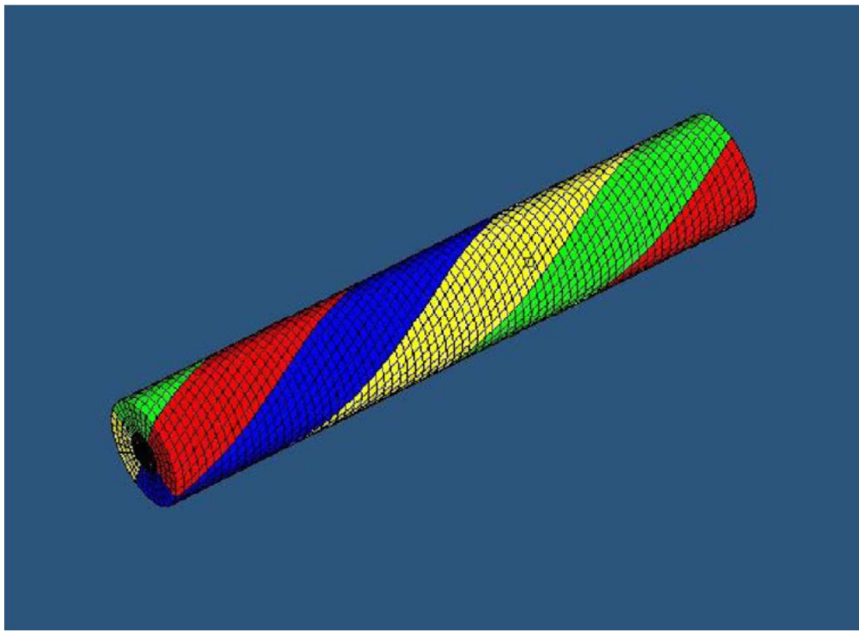

Figure 2-3: Isometric view of model geometry.

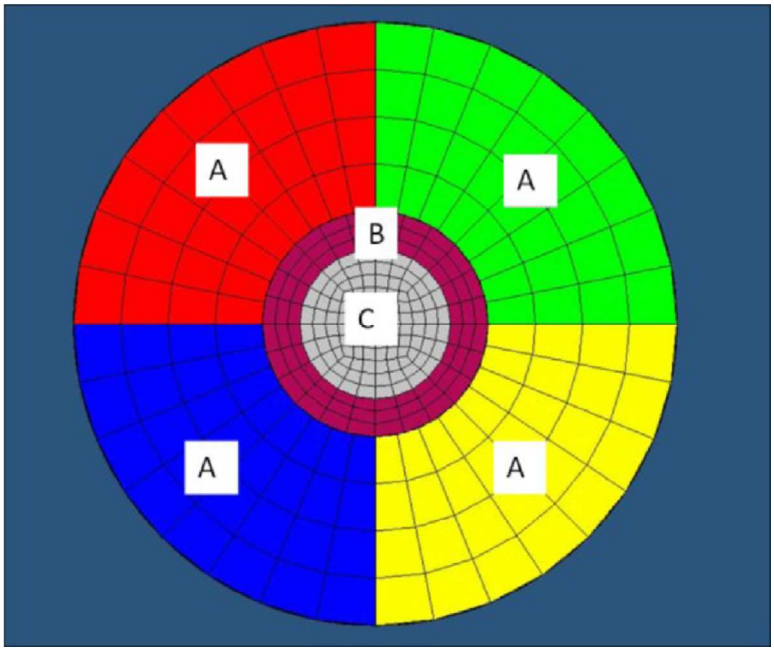

Figure 2-4: Cross-section of finite element model, (A) aluminum strands, (B) glass/epoxy, (C) carbon/epoxy.

2.3.2 Modeled geometry

The simplified model of the ACCC® consisted of four trapezoidal aluminum strands wound helically around a composite rod core. Non-linear geometries were taken into

account to accommodate contact interactions and plastic strains. The cross section of the model is shown in Figure 2-4, while Figure 2-3 shows an isometric view of the conductor model. Colors indicate individual components. The outer diameter of the wound aluminum strands (A) was 28.2mm, and the hybrid composite core had $\phi 6.35mm$ of carbon/epoxy (C) surrounded by an additional 1.60mm of ECR-glass/epoxy (B) for an overall core $\phi 9.53mm$. All components consisted of 8 noded linear brick, reduced integration continuum (C3D8R) elements. The interface between the glass and carbon composites was modeled as perfectly bonded by making their coincident nodes equivalent. The outer strands followed a helical spiral path having a pitch, $p = 152.4\ mm$ and length, $l = 152.4\ mm$, as shown in Figure 2-3. Surface interactions in the model used surface-to-surface contact penalty formulation and friction coefficients of aluminum on aluminum, $\mu_{Al-Al} = 1.1$, and aluminum on glass/epoxy composite, $\mu_{Al-ECR} = 0.5$ [22].

Outside of the 3-D model of the central portion of the conductor (152mm in length) the remaining lengths on both sides of the conductor were modeled as sets of rigid and elastic beams. Rigid beams 50mm in length connected each node on the face of the composite hybrid rod and aluminum strands to an isotropic elastic 2-node linear beam element (B31) 504.83mm long as shown in Figure 2-5. The use of the rigid and elastic beams and the central 3-D section approximate a continuous structure having a length equal to that of the experimental conditions.

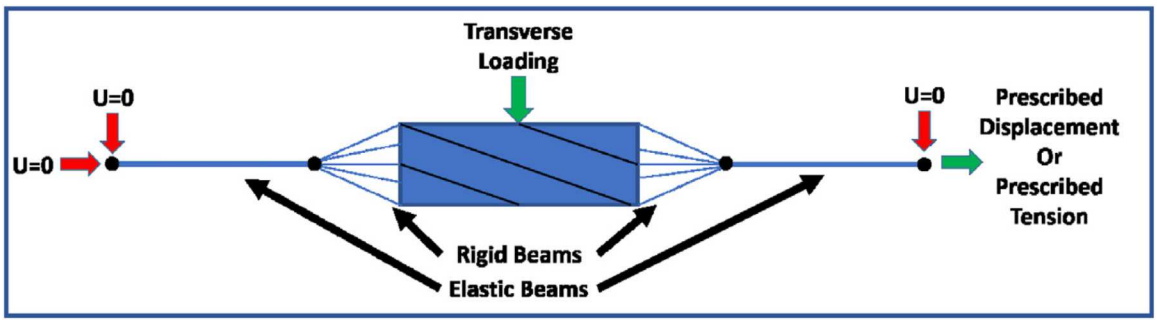

Figure 2-5: Boundary and load conditions for numerical analysis.

Orthotropic material properties of the hybrid composite rod were calculated using the elastic transversely isotropic Eshelby method [23] with a fiber fraction of $f = 0.6$ and the constituent properties shown in Table 2.1. An isotropic elastic-plastic with isotropic strain hardening material model was used for the 1350-O Al. Material properties used for the aluminum were determined experimentally with the values given in Table 2.2, with elastic-plastic behavior defined by the experimental true stress/strain curve of Figure 2-6.

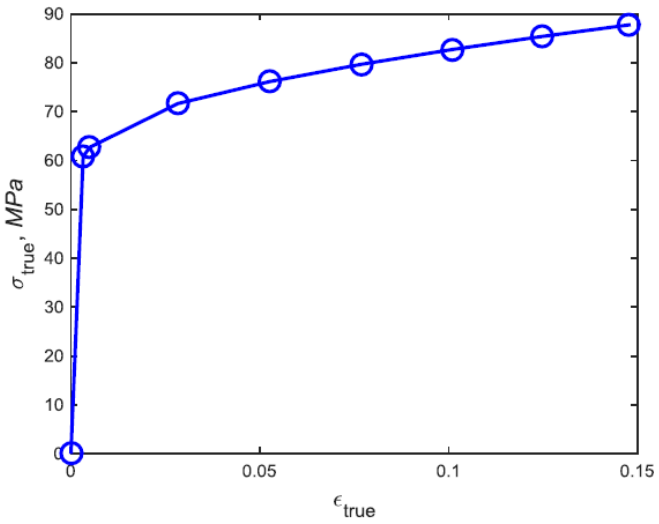

Figure 2-6: 1350-O Aluminum material model used in finite element analysis.

Table 2.1: Constituent material properties used to determine composite material properties [17].

Property	Carbon fiber	ECR-Glass fiber	Epoxy resin
Axial Young's modulus, GPa	230	76	3.6
Transverse Young's modulus, GPa	12	76	3.3
Longitudinal Poisson's ratio	0.3	0.22	0.2
Transverse Poisson's ratio	0.2	0.22	0.2
Longitudinal shear modulus, GPa	5.0	6.9	1.2

Table 2.2: Measured aluminum tensile properties of ACCC® conductor strands.

Property	1350-O Al
Young's modulus, E, GPa	48.5
Poisson's ratio, ν	0.33
Yield stress, σ_y, MPa	60.7

2.3.3 Static analysis

The implicit finite element method was used in the Abaqus/Standard® v.6.13.1 finite element solver to model the simplified ACCC® conductor section subjected to axial tension and transverse loading. Analyses were performed to investigate conductor response under different boundary conditions of prescribed displacements and prescribed tension, as shown by Figure 2-5.

First, a load or displacement was applied in the longitudinal direction at the elastic beam ends to create initial axial tensions of 11.47 kN, 17.20 kN, 25.80 kN, 34.40 kN, and 43.00 kN. Then, a transverse load of 1.00 kN was applied at the center of the model with a cylindrical analytical rigid surface of $\phi 41.30\ mm$, oriented orthogonal to the conductor.

In the static analysis, conductor deflections were predicted and compared with the static bending tests. Energy dissipations by friction, plastic deformations and recoverable energy were also evaluated for the different boundary conditions.

2.3.4 Dynamic analysis

To examine the dynamic response of the simplified conductor, the numerical model was expanded into an explicit dynamic analysis response to low-velocity impacts. The numerical model was constrained at the ends of the elastic beams with various prescribed displacements. An analytical rigid surface having a geometry, mass, and velocity equivalent to that of the experimental conditions then impacted the conductor. Then, the corresponding deflection and the total dissipated kinetic energy of the impactor were determined and compared with the experiment.

2.4 Experiment results and discussion

2.4.1 3-Point impact experiments

Seven samples of the ACCC® conductor were tested under a 3-point impact condition with no displacement or tension constraints at conductor ends. The impacting surface left a barely noticeable indentation at the point of contact but a significant amount of separation and deformation in the outer aluminum strands, as shown in Figure 2-7. Of the seven samples, three exhibited a significant degree of permanent curvature (about 90°) after impact, represented in Figure 2-7B. Closer examination of those samples revealed severe collapse of their composite rods evident through the aluminum stranding.

In the four tests in which the composite core did not collapse, the angular velocity decreased to zero while the pendulum kinetic energy was transferred into the conductor. The kinetic energy went to elastic strain energy of the composite rod, elastic and plastic strain energy in the aluminum strands, frictional dissipation energy between the strands and core, and frictional dissipation energy of the conductor sliding on the support posts. In addition, the energy also went into vibration of the pendulum arm and test frame,

friction in the pendulum bearings, air resistance of the pendulum, and the motion of the conductor sample through the air after impact. In these four tests the conductor stored a significant amount of recoverable strain energy in the bending of the composite core which upon straightening was transferred back into the pendulum to change its direction and overcome the friction of the support posts.

In the three tests which resulted in rod collapse, rod failures resulted in an unrecoverable transference of energy into rod fracture; the remaining energy that would have gone to the rod likely went into elastic and plastic strain energy of the aluminum strands, evident in the significantly greater permanent curvature.

The results of both the intact and collapsed rods of Figure 2-8 suggest that the given boundary and loading conditions used in the impact testing determine the transition point of failure. Catastrophic failures of the rods are most likely caused by excessive bending and the kinking type of failure of the carbon fibers on the compressive side of the rod. As mentioned before, this type of catastrophic failure of the ACCC® rods has been previously observed under static conditions by Burks et al in Refs [17] and [18]. When the compressive strength of the carbon fiber composite was not exceeded, the rods did not collapse and the conductors recovered after impact.

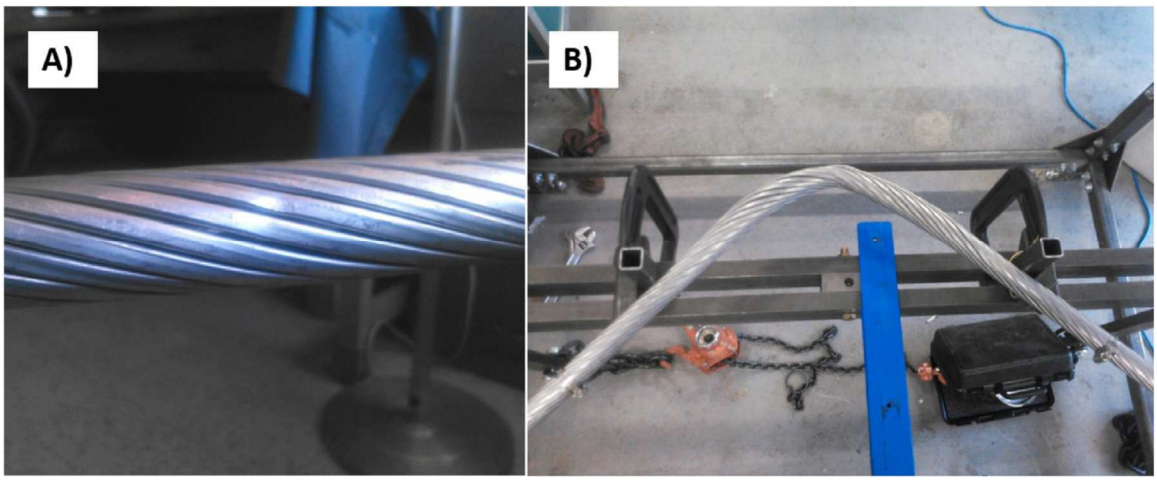

Figure 2-7: 3-point impact zone images: (A) intact core, (B) collapsed core.

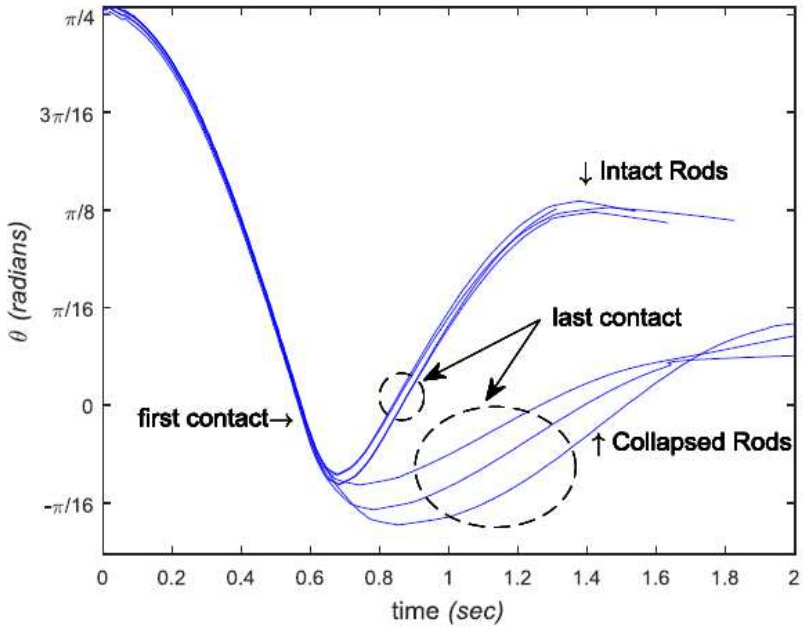

Figure 2-8: Angular positions in 3-point free ends impact experiments resulting in three collapsed core rods and four intact core rods.

2.4.2 Impact experiments under tension

In all of the tensioned impact experiments, the angular velocity decreased to zero while the pendulum's kinetic energy was transferred into the sample as elastic strain energy of the composite rod, elastic and plastic strain energies in the aluminum, and

frictional dissipation energy between all components. The impacting surface left a noticeable indentation and in the lower tension tests a small amount of separation visible in the outer aluminum strands, as shown in Figure 2-9. Starting at the point where the pendulum angular velocity was zero, the recoverable strain energy of the sample straightened the conductor and was transferred back into the pendulum reversing its direction and increasing its magnitude. Figure 2-9 shows examples of the impact damage to the aluminum for several of the tests at low, medium, and high tensions, whereas Figure 2-10 shows the angular positions as a function of time for the corresponding tests.

In Figure 2-11 the dissipated energy for each test is plotted as a percentage of the initial kinetic energy in the pendulum with respect to the initial axial tension from all tests. The resulting permanent curvature of the 3-point impact and tensioned conductor samples after removal of conductor clamps is shown in Figure 2-12, with the 3-point impact specimens on the left and applied tension increasing from left to right. The results from each tension test indicate significant repeatability.

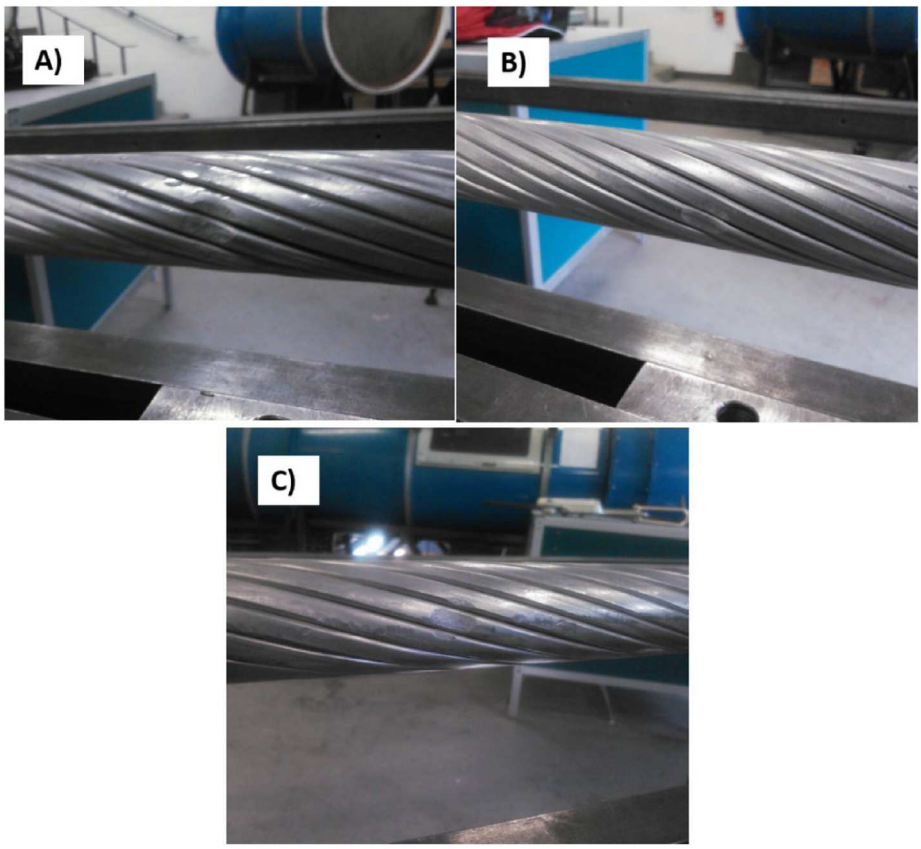

Figure 2-9: Impact zone images from tensioned impact tests: (A) low tension of 1.15 kN, (B) medium tension of 11.5 kN, (C) high tension of 29.2 kN.

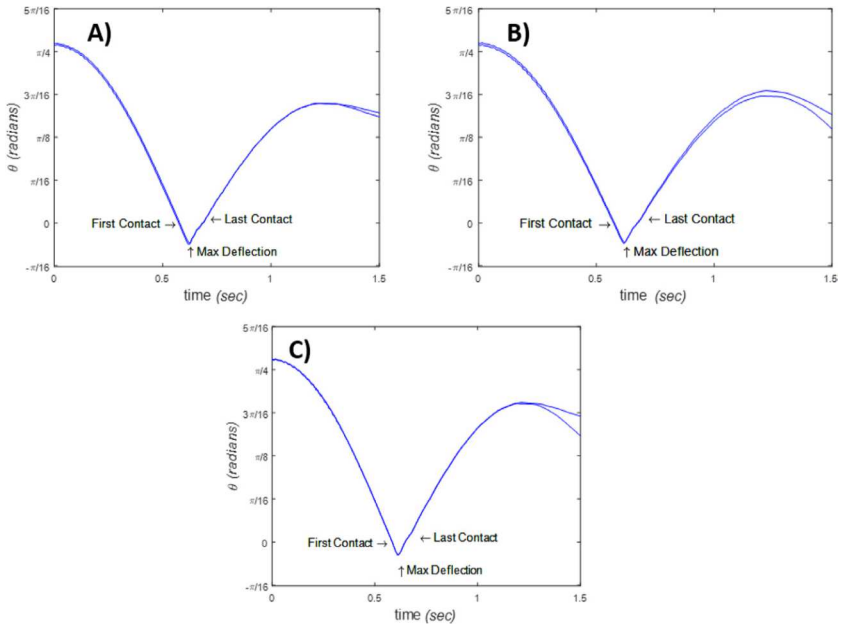

Figure 2-10:Angular positions during tensioned impact tests: (A) low tension of 1.15 kN, (B) medium tension of 11.5 kN, (C) high tension of 29.2 kN.

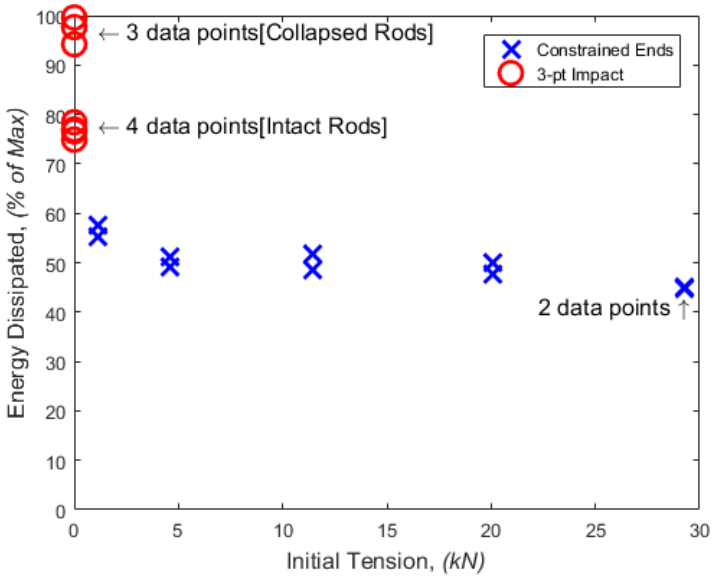

Figure 2-11: Percentage of energy dissipated after impact.

Figure 2-12: Resulting deformation of tested conductors.

2.5 Numerical results and discussion

2.5.1 Static analysis

The deflections under static loading conditions with prescribed displacements are given in Figure 2-13 for both the experimental and numerical transverse loads of 1.00 kN. It can be seen that under static conditions, the simplified numerical model reasonably estimates deflections with an average percent difference of 16.1%. This positive finding is important considering that the model included only 1/8th of the actual conductor, approximating the rest with simplistic elastic and rigid links.

For the prescribed displacement and tension boundary conditions, the total recoverable strain energy, plastic dissipation energy, and frictional dissipation energy from the static model are plotted in Figure 2-14, Figure 2-15, and Figure 2-16, respectively. As the transverse load is applied, the energies increase with deflection until the maximum is attained. For each quantity only small differences in energies are observed between the two boundary conditions. Prescribed tension provides more overall deflection while prescribed displacements result in greater energy values for a given initial axial load. Additionally, as the ratio of transverse load to initial tension decreases, the shift in energies and deflections between the two boundary conditions becomes negligible, suggesting that under relatively large axial to transverse load ratios, either boundary condition can be used to model the conductor response in service. In addition, the relative magnitudes of both the plastic and frictional dissipation energies are significantly smaller than the recoverable (or elastic) energy associated with static loading of the simplistic model considered in this study.

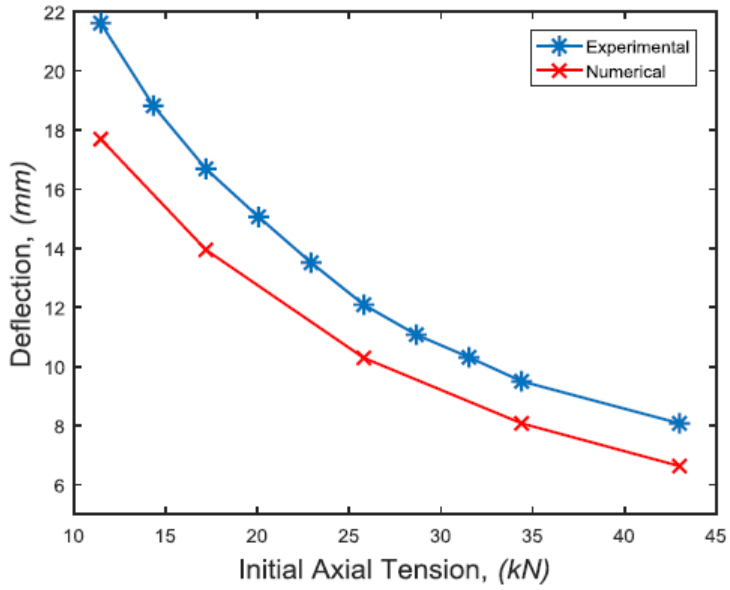

Figure 2-13: Experimental and numerical conductor deflections subjected to static transverse loading of 1 kN as a function of initial axial tension with prescribed displacement ends.

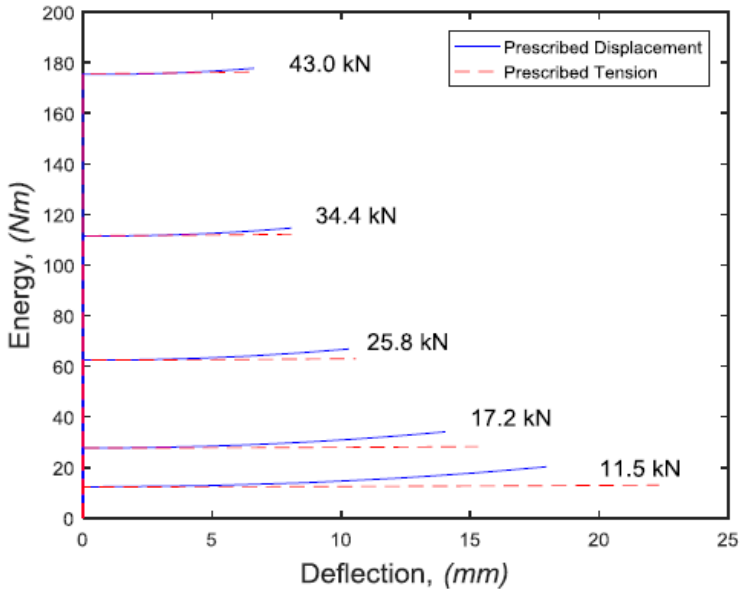

Figure 2-14: Total recoverable energy under transverse loading of 1 kN; static model.

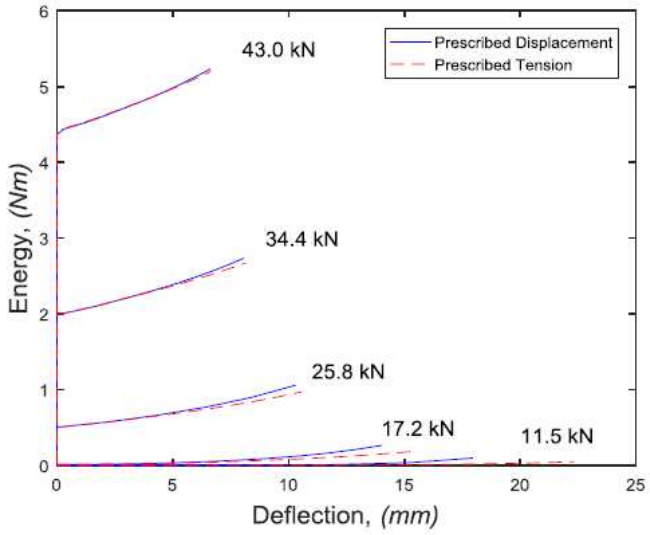

Figure 2-15: Total plastic dissipation energy under transverse loading of 1 kN; static model.

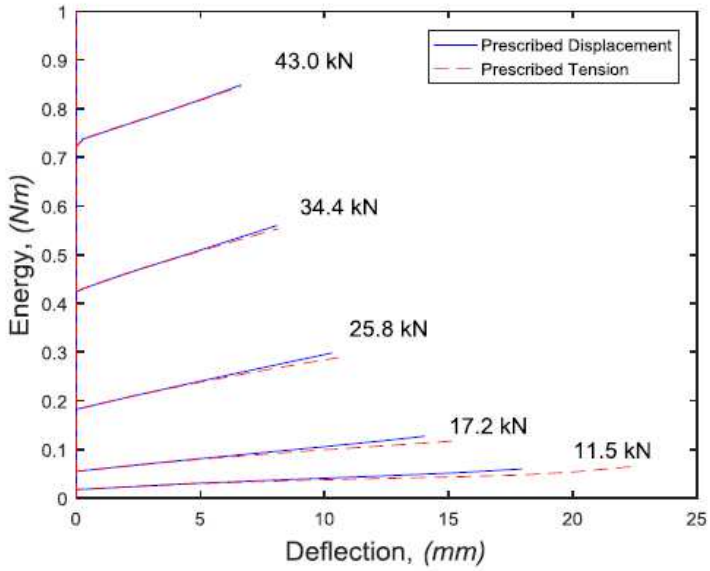

Figure 2-16: Total frictional dissipation energy under transverse loading of 1 kN; static model.

2.5.2 Dynamic analysis

After the static numerical analysis was found to provide a reasonable approximation under conditions similar to the experiment, a series of dynamic simulations were performed to evaluate the effect of axial tension on the deflection and total energy dissipated in the impact testing. Overall, the dynamic simulation did not provide high

quality replication of the experiment using the simplified model with the combination of rigid and elastic beams. As an example, for a prescribed displacement analysis with an axial load of 4.10 kN, the errors in the predictions of conductor deflections and total energy dissipated were found to be about 50% and 108%, respectively. Possible reasons for these discrepancies include absence of plasticity outside the central modeled conductor section, the use of fewer large aluminum strands, and the use of rigid links to connect the hybrid core to the elastic beam.

2.6 Suitability of proposed method for impact testing of HV conductors

The experimental work represents the first published laboratory testing of a HV transmission line conductor exposed to low-velocity transverse impact. It created a unique set of data which should help the manufacturers and users understand the response of ACCC® conductors to transverse impact. The specially designed and built impact test fixture produced repeatable results for impacting energies up to 250Nm with a cylindrical impacting surface having a velocity of 3.05m/s and boundary conditions of 3-point impact or initial axial tension from 1.15 kN to 29.2 kN.

The impact tests resulted in dissipated energies ranging from 109Nm (constrained ends with axial tension of 29.2 kN) to 240Nm (3-point impact and no axial tension). With an increase in axial tension, the dissipated energy was observed to approach a constant value. The tested samples of ACCC® showed more resistance to low-velocity transverse impact under constrained end conditions with initial axial tension, similar to that experienced in-service; no samples tested under such conditions resulted in rod failure. It was also observed that the ACCC® design is susceptible to severe damage of the composite core if the ends of the conductor are left free in the fixture, similar to

constraints during installation. Three out of seven samples tested with unconstrained ends resulted in composite rod collapse caused by the kinking of carbon fibers by excessive axial compression [17], [18]. This could indicate that ACCC® conductors with relatively moderate constraints during installations could develop severe rod damage by excessive bending if exposed to transverse impacts. This effect, of course, is strongly dependent on the length of the conductor subjected to impact, which was not investigated in this research.

Under the 3-point impact condition (unconstrained ends), four tests resulted in an average 140Nm of dissipated energy (no discernible rod collapse) and three with 239Nm (apparent rod collapse). Therefore, for the assumed impact energy and the length of the samples, this situation could be a transition for ACCC® to fail by excessive bending and rod collapse, or by less severe failure modes observed under the constrained ends with tension. It can be expected that this transition range will be dependent on the length of the span and impact situations.

Visible permanent damage to aluminum stranding is more evident after 3-point impact (no end constraints) with a greater separation of strands caused by plastic strain and a greater degree of permanent curvature than under axial constraints. For fixed end constraints, ACCC® exhibits significantly less permanent deformation of aluminum strands in comparison with the free end condition, and the damage to the strands seems to get less noticeable as the initial tension increases. This could suggest that transversely impacting objects could generate much less visible damage to the strands if the conductor is under large axial tension as in service. It should also be stated that under large axial loads and constrained ends, large impact energies to the conductor could cause severe

damage to the rods, not visible from the outside. However, this effect was not evaluated in this work due to the limitations of the fixture.

The numerical analyses presented in this study only approximate the experimental setup to help understand how energy dissipation depends on boundary conditions, and how the dissipated energy is distributed across the frictional, plastic and recoverable energies. The overall modeled geometry represents that of the experimental samples, but was simplified by the number of strands and the length of the specimens. Therefore, the numerical and experimental results are expected to illustrate similar trends and dependencies, but not match exactly. Despite its limitations, however, the static model generated quite close predictions of conductor deflections for a transverse load of 1.0 kN. The same model used under dynamic conditions resulted in significant errors in the prediction of both deflections and dissipated energies under impact. Clearly much more research is still required to fully understand the dynamic effects in long conductors if modeled using simplistic structures involving links and beams.

2.7 Chapter conclusions

The research presented in this chapter was conducted in an attempt to identify for the first time the most damaging conditions to one type of HTLS conductor subjected to low-velocity impact and determine its impact damage tolerance under laboratory conditions. This was successfully accomplished by testing one particular HTLS conductor in a purposely designed impact fixture that produced highly repeatable results. For the impact energies tested, ACCC® showed greater resistance to damage when constrained under tension in a fixed displacement state, similar to in service conditions. The only catastrophic rod failures occurred with the conductor impacted under zero tension and no

axial constraint, a situation potentially similar to conditions experienced during installation. Catastrophic rod failures that might occur under tension were not observed at tensions and energies tested. Achieving these failure modes will require enhancements to the test fixture to allow for higher impact energies and tensions.

As a simplified representation of a complex next generation conductor, the numerical model developed in this project performed reasonably well for the given static loading conditions. For the boundary conditions of prescribed displacements and prescribed tensions, the results showed little differences in energy dissipation and deflections under initially high axial tensions. Under dynamic loading conditions, however, the current model did not approximate the experimental results with reasonable agreement.

Overall, this research succeeded in identifying practical conditions that could be most damaging to the ACCC® conductor. The results should allow the manufacturers and installers of other HTLS conductors to identify and try to avoid potentially catastrophic circumstances during installation and in service.

3 Effect of fiber misalignment on bending strength of pultruded hybrid polymer matrix composite rods subjected to bending and tension

3.1 Introduction

Fiber hybridization is well known to improve the flexural performance of carbon fiber reinforced PMCs [24]–[28]; however, previous research has extensively shown that excessive bending without axial tension can still cause significant damage to the composite core [17]–[21], [29]–[31]. Kink bands observed in the carbon composite and experimental measurement of the uniaxial compressive strength suggest that bending damage initiates with micro-buckling from compressive stress in the carbon composite section. The subsequent formation of kink bands is well known to be the reason why carbon fiber reinforced polymers often exhibit lower compressive strength compared to their tensile strength [32]–[37]. This reduction varies considerably among the different carbon fiber types with 25% to 40% typical for the commonly available standard modulus and intermediate modulus fiber grades, respectively.

The addition of axial tension, however, has been shown to increase the ACCC® conductor's resistance to bending damage (see Chapter 2), [30], [31]. Waters [30] found with increasing axial constraint of the conductor, the typical damage from three-point impact in Figure 2-12 could be significantly reduced or avoided entirely. Three of the seven conductors tested with no axial constraint exhibited structural collapse of the

internal composite rod. The energy dissipated by the conductor in tensioned three- point impact experiments significantly decreased in Figure 2-11 with axial constraint.

It is well known that fiber misalignment and fiber bundle waviness have a detrimental effect on the axial compressive strengths of unidirectional composites [38]–[40]. Additionally, the non-linear behavior of carbon fibers could influence the predicted compressive strength of unidirectional composites subject to kink bands [41]. These effects were not considered in the present study since the influence becomes negligible for misalignment greater than 1° [42]. However, the fundamental influence of axial tension and fiber misalignment on the damage initiation of composite cores subjected to bending had yet to be investigated before this research.

3.2 Methods

3.2.1 Finite element model

The numerical model of a composite core in Figure 3-1 consists of C3D8R and C3D6 solid continuum elements in Abaqus 2017/Standard with a uniform axial element length of 0.56 mm. The analysis used the composite material elastic constants in Table 3.1 calculated using the Mori–Tanaka Eshelby formulation [23], [43] with volume fiber fractions of 0.64 and 0.69 for the glass and carbon sections, respectively [44], [45]. Non-linear geometries were used to account for large deformations. The interface at the carbon and glass sections share coincident nodes for perfect bonding.

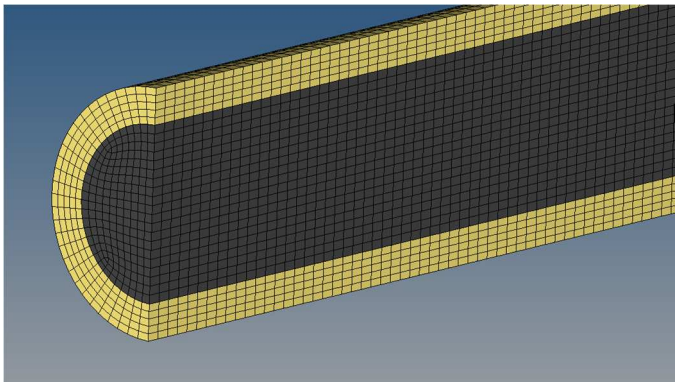

Figure 3-1: Finite element mesh of composite core.

Table 3.1: Constituent material properties for composite core components [43], [46]–[49].

	Glass/Epoxy	Carbon/Epoxy
	Composite	**Composite**
E_1(GPa)	49.3	159.6
E_2(GPa), E_3(GPa)	9.27	7.37
ν_{12}, ν_{13}	0.052	0.012
ν_{23}	0.545	0.478
G_{12}(GPa), G_{13}(GPa)	5.25	3.97
G_{23}(GPa)	4.74	3.12

Three analyses were performed using friction-less analytical rigid surfaces to apply loading and constraints to simulate three-point bending (Figure 3-2a), four-point bending (Figure 3-2b), and combined tension bending around a mandrel (Figure 3-2c). The analysis of combined bending with tension simulates transportation and installation conditions and consists of a 381 mm long Drake size rod formed around rigid mandrels having diameters of 381 mm, 467 mm, 561 mm, 762 mm, 1270 mm, and 2000 mm by applying a follower surface shear traction sufficient to fully wrap the rod around the mandrel. Additionally, axial tensions of 0.00 kN, 22.24 kN, 44.48 kN, and 88.96 kN were imposed by a surface normal traction that rotates with the model geometry.

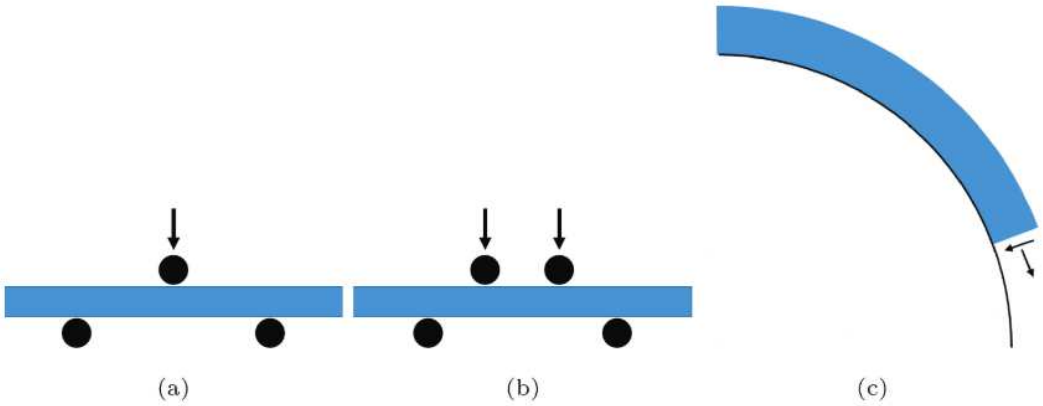

Figure 3-2: Numerical models: (a) three-point bending, (b) four-point bending, (c) mandrel bending.

3.2.2 Analytic solution

Using the principle of superposition, Eq. (3.1) provides a simplified linear-elastic approximation of the longitudinal stress component σ_1 due to the stress contributions from pure bending and axial tension. This idealized case is most representative of pulling a conductor over an installation guide pulley or wrapping around a mandrel.

$$\sigma_1 = \sigma_{bend} + \sigma_{tension} \quad (3.1)$$

Given the bend radius R of the neutral plane and the distance y from the neutral plane, the bending stress σ_{bend} is given simply by classical beam theory as Eq. (3.2). E_1' indicates the elastic modulus of the respective material section.

$$\sigma'_{bend}(y) = \frac{E'_1 y}{R} \quad (3.2)$$

The axial stress due to tension in each section $\sigma'_{tension}$ was approximated using the general rule of mixtures in Eq. (3.3).

$$\sigma'_{tension} = \frac{E'_1 \sigma_1}{E_1} = E'_1 \epsilon_1 \quad (3.3)$$

Where E_1 is the average stiffness of the hybrid rod ($E_1 = 104.5\ GPa$), σ_1 is the average stress imposed by a given axial tension, and ϵ_1 is the average strain due to tension. E_1' is dependent on y such that the appropriate section parameters were used in Eq. (3.2) and Eq. (3.3).

$$E_1' = \begin{cases} E_1^{carbon}, & -3.37mm \le y \le 3.37mm \\ E_1^{glass}, & -4.765mm \le y < -3.37mm, \quad 3.37mm < y \le 4.765mm \end{cases}$$

3.2.3 Experimental

Experimental flexure testing was performed to validate the results of the finite element analysis in four- and three-point bending. Using the bend fixture and loading pins specially designed by Burks [18] with an outer span length of 304.8 mm and a load span one-third the support span in the 4-point configuration. A span-to-depth ratio of 32 was used to minimize shear failures resulting from the highly orthotropic nature of the composite [18], [50]. Drake sized rods [51] received from CTC Global were cut to lengths of 381 mm, and PTFE tape was applied to the rod at the load and support pin locations to reduce contact stress and minimize the influence of the pins in a non-ideal test. Seven rods were used in three-point bending and three in in the four-point tests. Specimens were loaded transversely with no axial constraint at 3 mm/min to failure on an Instron 5982 dual column floor frame. Failed PMC rod specimens were vacuum infiltrated with Buehler Epoxicure™ 2 to stabilize the fractured surfaces for sectioning. A Buehler IsoMet™ 15HC diamond wafering blade was then used with a low-speed saw to cut the specimens on a plane orthogonal to the direction of the applied bending load. Final polishing was performed with a 0.05 μm alumina suspension and images were acquired with a JEOL 5800LV scanning electron microscope.

3.3 Hybrid rods subjected to idealized bending

3.3.1 Criteria for axial tensile and compressive failure

In combined bending and tension, shear is neglected and failure is assumed to initiate at one of the four locations in the hybrid composite rod with the greatest magnitude of stress in the fiber direction σ_1 (Figure 3-3):

1. Tensile failure at surface of glass section, y = 4.765 mm
2. Tensile failure of carbon at glass interface, y = 3.37 mm
3. Compressive failure of carbon at glass interface, y = −3.37 mm
4. Compressive failure at surface of glass section, y = −4.765 mm

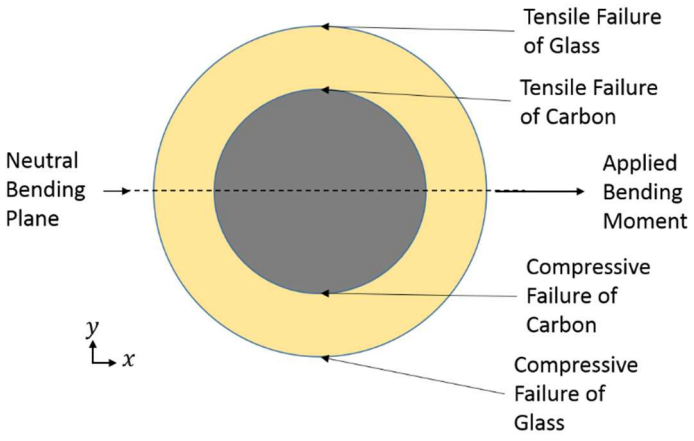

Figure 3-3: Assumed locations of failure initiation.

In Table 3.3, values for the tensile strength S_{11}^{+} in the fiber direction were calculated by the simple rule of mixtures with the constituent properties in Table 3.2 [43]. The axial compressive strengths, S_{11}^{-}, were calculated using the modified Lo & Chim model based on micro-buckling of a Timoshenko beam [52], [53] (Eq. (3.4)) as a function of the longitudinal shear modulus G_{12} and longitudinal Young's modulus E_{11} of the composite in Table 3.1. Eq. (3.4) is an analytical semi-empirical predictor of unidirectional

composite compression strength where β is a dimensionless parameter empirically calibrated to fit the experimental data of the first kink response in a specific material system. From experimental data of the uniaxial compressive stress at the initial formation of fiber kinking, Breiman determined β for E-glass reinforced polymers β = 6.231, and for high strength carbon fiber reinforced polymers β = 5.195 [53]. Additionally, the carbon/epoxy flexure stress at which significant acoustic emissions were detected by Burks [18] is included. Due to the stress gradient in bending, support and constraint from surrounding carbon or glass fibers not exposed to their critical buckling strength results in measured bending compressive strengths exceeding those of unidirectional compressive strengths [34], [54].Thus, a greater measured compressive stress to initiate micro-buckling and resulting acoustic emission events in bending is expected when compared to the predicted strength calculated using Eq. (3.4).

$$S_{11}^{-} = \frac{G_{12}}{1.5 + 12\left(\frac{\beta}{\pi}\right)^{2}\left(\frac{G_{12}}{E_{11}}\right)} \tag{3.4}$$

Table 3.2: Constituent tensile axial strength properties.

	Epoxy [46]	ECR-Glass [55]	T700S carbon [49]
Tensile modulus (GPa)	2.27	72.3	230
Failure strain (%)	5.6	4.8	2.1

Table 3.3: Composite axial strength properties for damage initiation.

	Glass/Epoxy Composite	Carbon/Epoxy Composite
S_{11}^{+} (GPa)	2.24	3.39
S_{11}^{-} (GPa)	0.805[a]	1.71[a],1.75[b]

[a] Modified Lo & Chim [52], [53],
[b] Burks [18] onset of acoustic emissions

3.3.2 Analytical and numerical results

Substituting Eq. (3.3) and Eq. (3.2) into Eq. (3.1), the axial stress along the diameter of the composite rod as a function of bend radius R, applied load P, and cross-sectional area A can be expressed as Eq. (3.5). Figure 3-4 compares the axial stress along the cross-section under various tensions around a mandrel with curvature of $1/R = 2.62\ m^{-1}$ (R = 381 mm) from the numerical model of tensioned bending and the analytical solution of Eq. (3.5). The discontinuity in axial stress at the carbon/glass interface (y = ±3.37 mm) is a result of the abrupt change in stiffness from the glass composite to the carbon composite regions. The analytic model does not account for non-linear effects and transverse contact with the mandrel and therefore produces an aggressive estimate of the loading combination to initiate glass compressive damage. The transverse compression imposed by contact with the mandrel at the glass surface (y = −4.765 mm) causes the FE results to deviate from the analytic solution of Eq. (3.5) for small diameter mandrels as tension increases. This discrepancy, however, becomes negligible further from the surface and with large bend diameters as the Brazier effect is less pronounced.

$$\sigma_1' = E_1'\left(\frac{y'}{R} + \frac{P}{E_1 A}\right) \tag{3.5}$$

$$\frac{1}{R} = \frac{1}{y'}\left(\frac{\sigma_1'}{E_1'} - \frac{P}{E_1 A}\right) \tag{3.6}$$

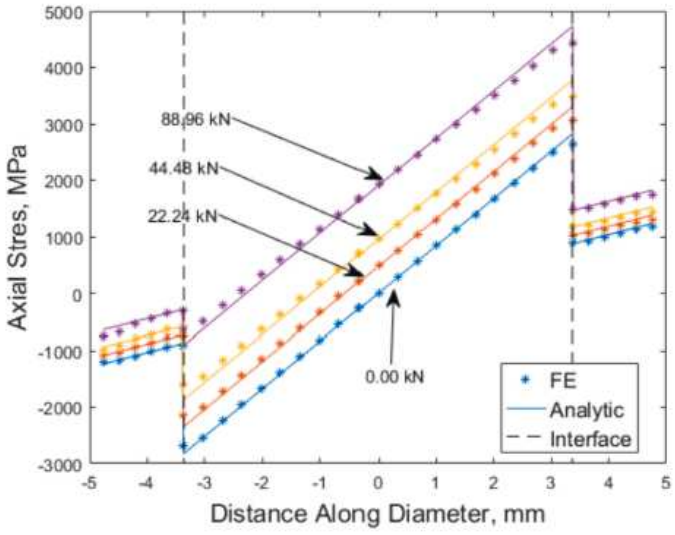

Figure 3-4: σ_{11} along diameter of rod for curvature 1/R = 2.62 m^{-1} and four different axial loads (indicated by arrows).

By rearranging Eq. (3.5) to produce Eq. (3.6) and substituting approximated composite strengths S_{11} from Table 3.3 for σ_1, an estimate can be made of the required axial load and curvature required to initiate damage in a 9.53 mm PMC core. For a perfect composite, Figure 3-5 shows the loading combinations required to achieve the failure criterion of Section 3.3.1 determined with the analytic approximation and finite element model. From an engineering perspective the most conservative constraints of analytic carbon compression, numeric glass compression, and analytic carbon tension from Figure 3-5 can be selected for safe combined loading. When the rod is subjected to bending without axial tension, carbon micro-buckling is predicted to initiate at a curvature of 3.19 m^{-1}, compared with the value at the onset of acoustic emissions measured by Burks of 3.57 m^{-1} [18]. This is a reasonably conservative estimate as it predicts micro-buckling damage initiating from slightly less curvature than actual results

from four-point bending experiments, bending diameter, D = 627 mm compared to D = 560 mm (error of 12%).

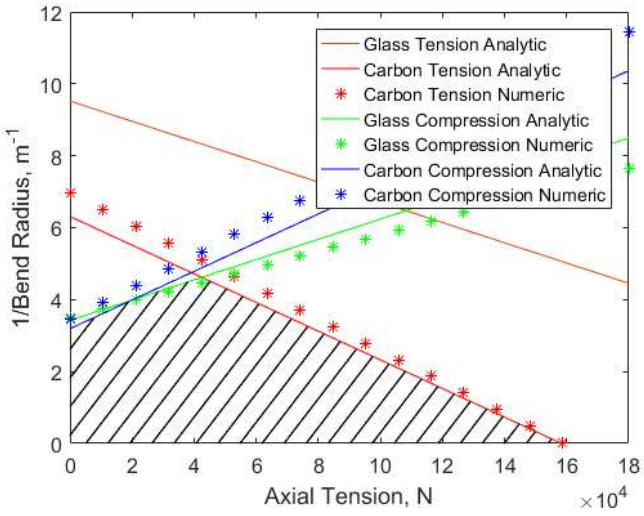

Figure 3-5: Predicted failure as a function of combined bending and tension. Hatch marks indicate safe region.

Increasing the axial tension as seen in Figure 3-5 offsets the contribution of bending to the carbon compressive stress. At 18 kN and curvature of 3.91 m^{-1}, conditions to initiate micro-buckling shift from the carbon composite at the interface to the glass composite at the exterior. This remains the predicted damage initiation mode until an axial tension of 44.8 kN when tensile stress in the carbon exceeds its predicted tensile strength at a curvature of 4.53 m^{-1}. Thus, near optimal resistance to bending damage is achieved at typical in-service tensile loads. Finally, for the case of axial tension with no bending, damage is predicted to occur at 158 kN compared to the experimentally measured failure load of 174 kN (error of 9%) [8]. The significantly lower axial modulus of the glass composite results in tensile stress well below its theoretical strength when the rod is subjected to combined bending and tension. Therefore, axial tensile failure in the glass composite is not predicted.

More detail on the methods to create Figure 3-4 and Figure 3-5 can be found in the Appendix.

3.4 Experimental validation

3.4.1 Failure characteristics from three- and four-point loading

The elastic model closely represents the experimental three- and four-point bending results in Figure 3-6a and b, respectively. Specimens with compressive fracture initiation apparent, as in Figure 3-7, were observed to fail in proximity to the loading pins. The applied bending loads are summarized in Table 3.4 with the maximum calculated stresses in the corresponding numerical analyses in Figure 3-8.

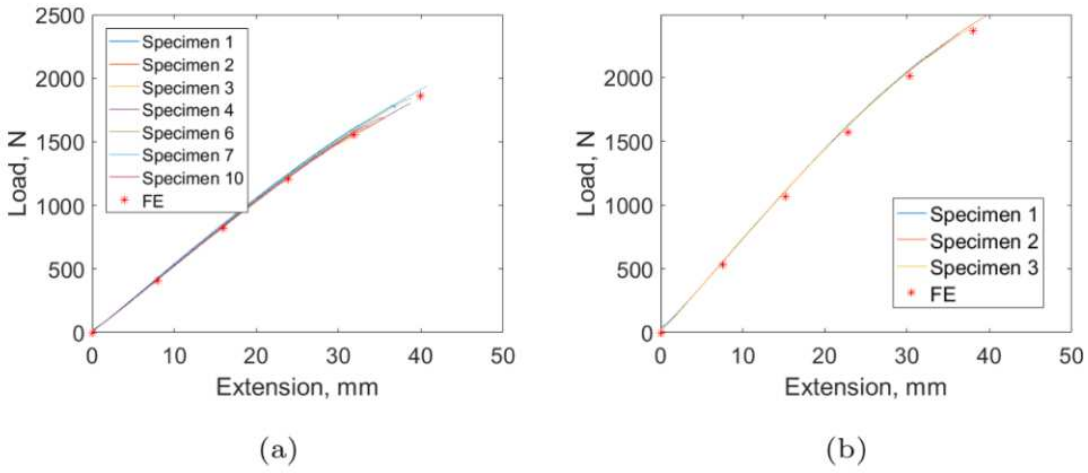

Figure 3-6: Experimental and numerical (a) three-point bending, (b) four-point bending. (Extension refers to transverse deflection of the rod)

Figure 3-7: Typical example of experimental failure proximal to loading pin in three-point and four-point bend experiments.

Table 3.4: Experimental loads and extensions at failures.

	Mean	Standard Deviation
Three-point failure load (N)	1766	102
Three-point failure Extension (mm)	37.2	2.3
Four-point failure load (N)	2414	74
Four-point failure Extension (mm)	38.0	1.6

Comparing Table 3.3 with Figure 3-8, the predicted compressive bending stress at which micro-buckling in the carbon composite begins is 75.8% (1.714 GPa / 2.261 GPa) of the mean compressive stress determined at catastrophic four-point bending failure and 69.7% (1.714 GPa / 2.458 GPa) at three-point bending ultimate failure. Between these events, the composite core provides no discernible visual evidence that permanent damage has developed or is evolving; in practice, visual inspection is not possible with the conductor's aluminum stranding. Traditional conductor designs utilize ductile

isotropic materials such as steel and exhibit a significant observable plastic response prior to ultimate failure.

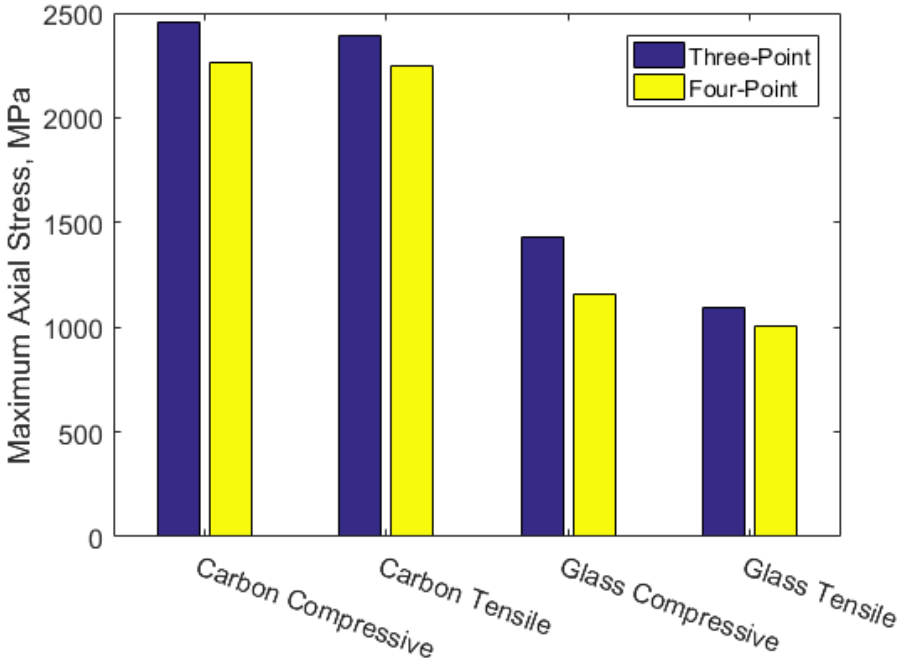

Figure 3-8: Numerically determined maximum axial stresses at experimental failure extension.

Determination of the maximum compressive strength of unidirectional composites with this type of flexure testing is highly influenced by the loading configuration and the stress distribution imposed. In Figure 3-8 the calculated stresses at failure are on average 175 MPa greater in three-point bending than four-point bending. When the composite rod is subjected to three-point bending the greatest magnitude of resulting axial stresses is localized to the region near the load pin with a significant gradient moving away from the pin; in four-point bending the axial stress is nearly uniform between the two inner loading pins. This effect of stress gradient on flexure strengths has been well explained [34], [54]. Additionally, the loading pins impose a stress field to flexure specimens that is more complex than the ideal case of wrapping around a mandrel. Three specimens tested in

three-point bending were sectioned near the mid-plane. Figure 3-9 is representative of all specimens failed in bending and shows the formation of carbon fiber kink bands with fiber fracture from shear mode micro-buckling (red arrows). Regions of cross- sectioned fibers showing an oval shape visible in Figure 3-9 were found in all fractured specimens and indicate probable out of plane fiber misalignment with kink band formation along these regions orthogonal to the plane of loading. Their proximity to in-plane fibers with no fracture suggests that the misalignment is not a product of shifting of the fractured pieces after failure. This type of misalignment was seen in both the carbon and glass regions of the composite rod. Additionally, evidence of significant in-plane carbon fiber misalignment (up to $\phi \approx 18^{\circ}$ measured with a protractor) in Figure 3-10 was found in clusters of fibers across all specimens and ranged in location from near the glass interface to the center of the PMC rod. Misalignment of the glass fibers was also observed throughout the thickness of the glass region.

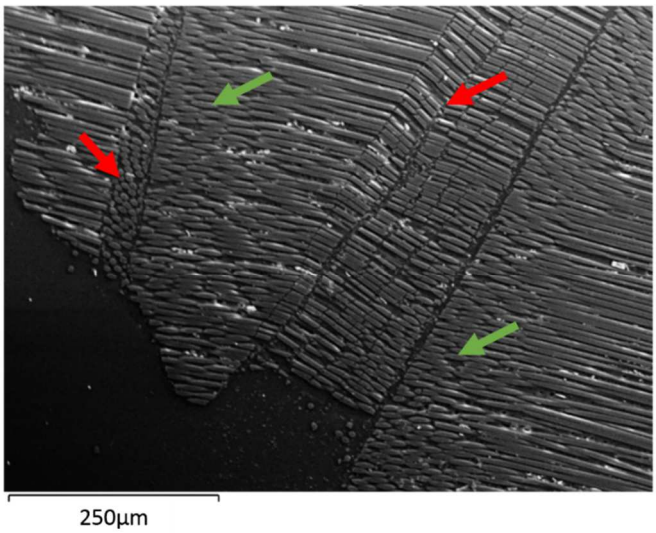

Figure 3-9: Kink zone in carbon/epoxy section near rod failure location in 3-point bending. Green arrows indicate out of plane fiber misalignment and red arrows indicate shear mode kink bands.

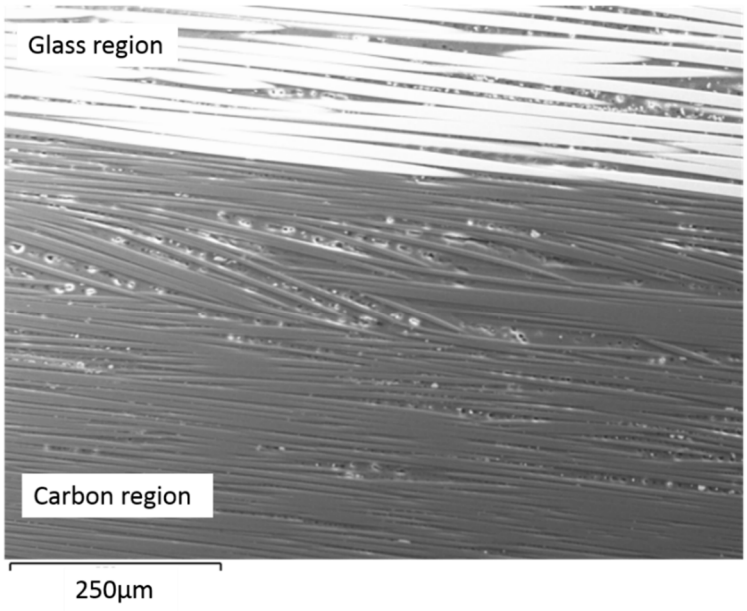

Figure 3-10: Carbon fiber and glass fiber misalignment in a composite core.

3.5 Effect of fiber misalignment on rod failures

The fiber misalignment observed in the hybrid composite rod can significantly affect compressive strengths making the PMC core more susceptible to bending damage [33], [34], [38], [56]. Depending on its location and severity, micro-buckling initiation could shift from the predicted regions of the perfect composite in Section 3.3.1 to other sites in the rod. Near the fracture region in Figure 3-11 no less than three distinct kink bands (indicated by red arrows) likely resulted from shear instabilities at different locations.

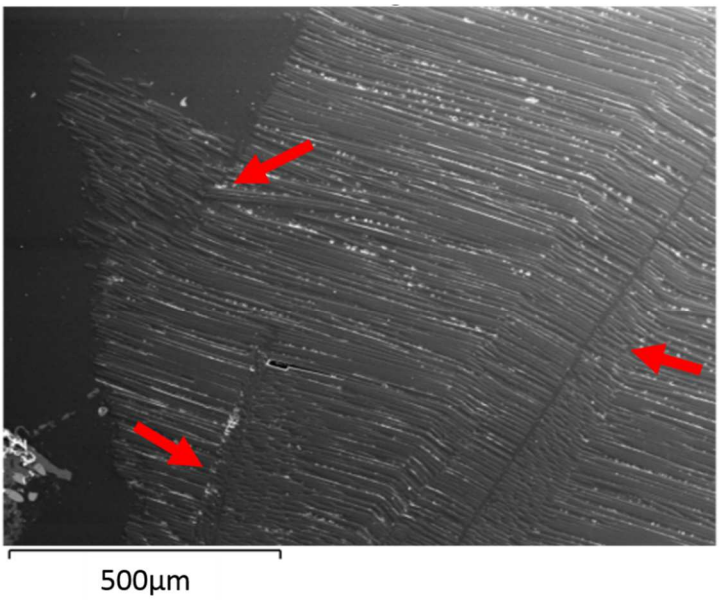

Figure 3-11: Multiple kink bands in carbon region near location of rod structural failure.

The effect of a uniform fiber misalignment on the compressive strength calculated via the modified Lo & Chim model was determined by applying Eq. (3.4) to a transformed coordinate system rotated around the 2-axis of the composite elastic constants of Table 3.1. The basis change of the anisotropic compliance tensor in matrix form, **S**, can be achieved by application of equation 3.7.

$$\boldsymbol{S}^{transformed} = K\boldsymbol{S}K^{-1} \tag{3.7}$$

With $c = cos\theta, s = sin\theta$ the rotation matrix, K, about the -2 direction, is given as follows:

$$\begin{bmatrix} c^2 & 0 & s^2 & 0 & 2cs & 0 \\ 0 & 1 & 0 & 0 & 0 & 0 \\ s^2 & 0 & c^2 & 0 & -2cs & 0 \\ 0 & 0 & 0 & c & 0 & -s \\ -cs & 0 & cs & 0 & c^2 - s^2 & 0 \\ 0 & 0 & 0 & s & 0 & c \end{bmatrix}$$

From this transformed compliance matrix $S^{transformed}$(equation 3.7) , values of G_{12} and E_{11} are derived. These values are then used in equation 3.4 to calculate the theoretical compressive strength of the misaligned composite.

This simple case assumes the fibers are parallel and uniformly misaligned across the specimen. Wisnom showed that for variable misalignment over short distances, as found in the hybrid composite rod, the maximum compressive stress to cause micro-buckling is influenced by the average more than the maximum angle of misalignment [33]. Using the compliance transformation relationships to determine the off-axis composite elastic components(ie., an average fiber misalignment), the compressive strengths can be predicted for the misaligned composites by the modified Lo & Chim model [52], [53] in Figure 3-12a. Fiber misalignment has a more profound effect on the compressive strength of the carbon composite as opposed to glass. For example, a 6° misalignment results in a 23% reduction in the theoretical compressive strength of the carbon composite while only a 12% reduction in the glass composite.

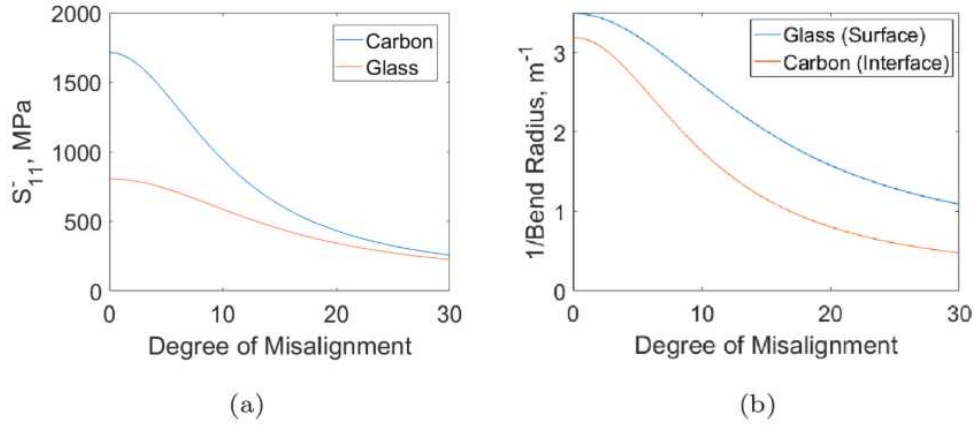

Figure 3-12: Influence of fiber misalignment on (a) composite axial compressive strengths, and (b) damage initiating bend curvature.

In the most susceptible case for micro-buckling, bending with no axial tension, Figure 3-12b displays the curvature predicted to initiate damage if an average fiber misalignment exists in the glass at the surface or in the carbon at the interface. This figure uses the more conservative carbon analytic and glass numeric predictions from Section 3.3.2. The maximum local carbon fiber misalignment of 18° observed in Figure 3-10 results in a predicted compressive strength of 496.3 MPa, approximately a 71% reduction from its nominal strength.

Applying this calculated strength to the same bending model, if this local misalignment existed at the interface and the point of maximum compression in bending, the bending model would predict micro-buckling initiation at a curvature of 0.92 m^{-1}, for the same reduction of 71%. Given the observed approximate location of this localized bundle 125 μm from the interface, the corresponding curvature to initiate micro-buckling would be 1.00 m^{-1}, a reduction of 69%. These reductions are worst case and do not account for any shear stabilization from nearby regions with less misalignment. Therefore, to fully understand the conditions leading to failure, many more observations of the fiber orientation throughout the composite core structure would be needed. While the maximum carbon fiber misalignment was 18° in Figure 3-10, the average misalignment is noticeably less. If, for example, the average fiber misalignment is assumed to be 6°, Figure 3-13 shows the damage initiating conditions when bending is combined with tension and fiber misalignment exists at the glass composite surface and carbon composite interface. The individual contributions of misalignment in the carbon composite and glass composite regions are shown in Figure 3-13b and c, respectively. The location of fiber misalignment has a profound effect on the predicted conditions for

damage initiation. Misalignment at the glass surface causes the predicted compressive damage initiation to shift from the carbon composite at the interface to the exterior surface of the rod in Figure 3-13c. If severe misalignment exists in the carbon section, compressive damage can initiate away from the interface towards the center of the rod.

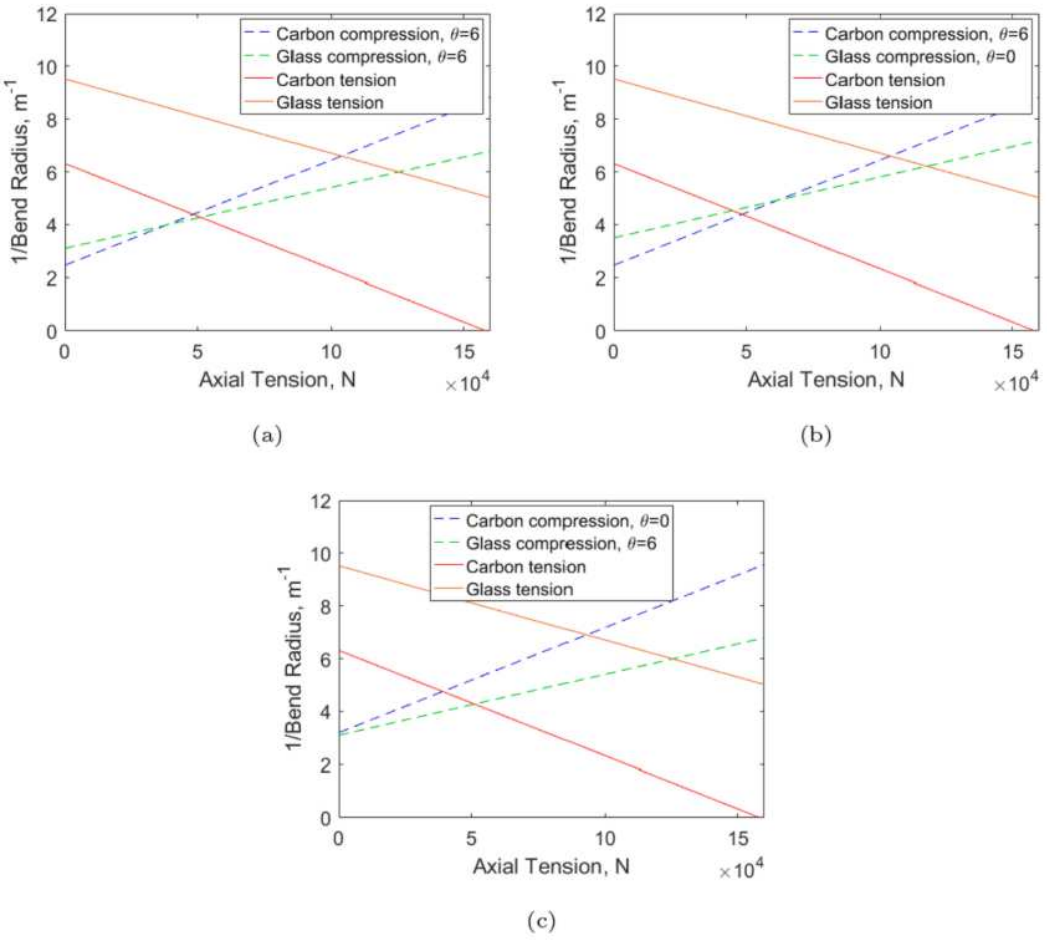

Figure 3-13: Damage initiating conditions predicted by bending model from Section 3.3.2 for assumed 6° fiber misalignment in (a) carbon region at interface and glass region at rod surface, (b) only carbon region at interface, and (c) only glass region at rod surface.

Figure 3-13 can also be used to determine the tension necessary to mitigate the impacts of fiber waviness. For example, in the case of misalignment in the carbon section, the effect of fiber waviness can be offset by the application of 18.4 kN of tension to produce the same damage initiating bend radius of 3.19 m^{-1}. Of course, if fiber

misalignment were reduced, composite cores could have an increased resistance to bending with a corresponding reduction in the critical minimum bending radius even without the application of tension.

3.6 Chapter conclusions

Ultimate failure of the ACCC® composite core conductor under pure bending is known to cause catastrophic rod collapse initiating in the lower axial compressive strength carbon composite region. The application of axial tension has been shown to reduce the critical bend radius. It has been shown numerically and analytically, that with increasing applied tension, damage initiation due to bending in a perfectly aligned composite can shift from micro-buckling in the carbon composite region to micro-buckling in the glass region. Further increases in axial tension will subsequently result in tensile failure modes of the carbon composite region.

Natural fiber misalignment present from the pultrusion manufacturing process has a strong influence on the bending strength of the composite core. The most probable location for compressive damage initiation and resulting kink band formation can shift away from the outer most carbon fibers and therefore must be considered in failure analysis. The compressive strength reduction due to fiber misalignment is most pronounced under pure bending; however, the addition of applied axial tension can mitigate this effect as failure shifts to a tensile mode.

A reduction in the amount of fiber misalignment is expected to improve the conductor's robustness during transportation and installation when bending is expected. If it is not feasible to improve the inherent fiber misalignment, application of axial tension can ameliorate its effect. Thus an installation tension of 20 kN increases the

curvature at the initiation of failure to 3.99 m^{-1} from 3.19 m^{-1}. Even with a 6 degree misalignment in the carbon, the same installation load provides additional protection against bending, increasing the critical curvature to 3.25 m^{-1}.

4 Monitoring of overhead transmission conductors subjected to static and impact loads using fiber Bragg grating sensors

4.1 Introduction

High-temperature low-sag conductors have been designed to operate in harsh and highly dynamic environments, and to last for many decades. During installation they can experience complex mechanical loads. In-service, they can be subjected to Aeolian vibrations, galloping, ice loading and shedding, and impacts from trees, or be targeted by vandalism. At present, monitoring transmission lines based either on traditional or HTLS conductors for mechanical problems caused by excessive in-service loads is very difficult or even impossible. A new ability to monitor the in-service structural response of HTLS conductors would be especially beneficial by reducing costs associated with maintenance and inspection, and improving the capability to perform life predictions on modern transmission systems.

In ACCC® the composite core of carbon/epoxy surrounded by a galvanic barrier of glass/epoxy provides structural support while the fully annealed aluminum conducts the electricity. Since the conductors are based on a glass/carbon hybrid composite rod with difficult to predict failure characteristics [8], [17]–[21], [29], [44], [46], [57], [58], monitoring ACCC® and other HTLS conductors is not straightforward. It has been shown that depending on the loading conditions, the conductors can lose their structural integrity in a catastrophic manner due to excessive bending upon impact (Figure 2-11,

[30]). Excessive bending could also occur during installation if the specific guidelines of the manufacturers are not followed.

Because of the high electrical potentials present on transmission lines, any measurement technology must utilize a sensor and signal immune to electromagnetic interference and be non-conducting to avoid grounding. For this reason, optical strain sensors that utilize Fiber Bragg Gratings (FBG) could be ideal for the static and dynamic monitoring of in-service overhead transmission lines. FBG sensors utilize a series of equally spaced gratings that are etched or by some other means written directly into an optical fiber without changing the size or geometry of the fiber [59]. Each set of gratings reflects a specific wavelength of light that varies as the fiber is strained or is subjected to a change in temperature, causing an alteration in the distance between gratings and in the index of refraction (see Figure 4-1) [60]. A typical sensor etched in the optical fiber is about 7mm long and contains several thousand gratings that collectively reflect about 30-80% of a particular wavelength of light [59]. An optical interrogator connected to a fiber with FBGs produces a broad spectrum of wavelengths and receives the return reflections. Depending on the capabilities of the interrogator, it is possible to read forty or more distinct sensors spread along a single fiber. Due to low attenuation in the optical fiber, signals can be read from sensors many kilometers away from the interrogator.

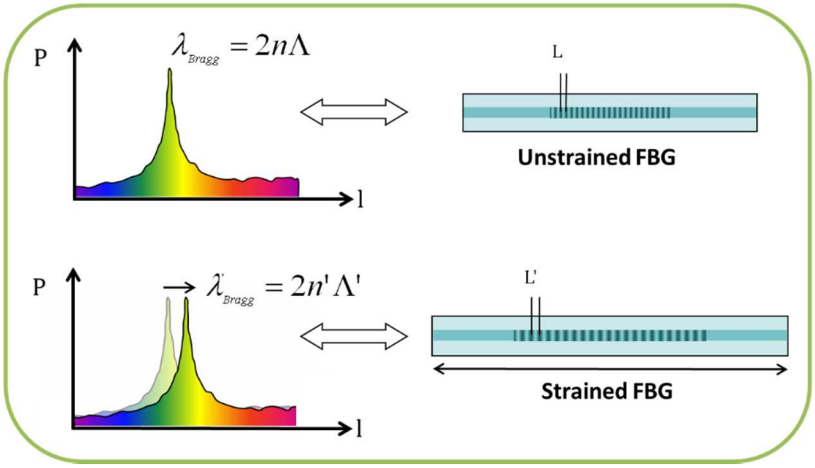

Figure 4-1: Reflected wavelength changes as fiber is strained [61]. *Where λ_{Bragg} is the central wavelength, n is the index of refraction, Λ is the period of the index of refraction variation of the FBG, P is the reflected wavelength intensity, and L is the FBG grating spacing.*

Previous work has used FBG sensors in load cell designs or other specialty devices incorporated in the hardware used to hang overhead transmission lines to measure conductor environmental loading indirectly, [62]–[67]. While one study has been published on the monitoring of traditional steel reinforced aluminum overhead conductors using FBGs epoxied to the surface of the outer aluminum strands [68], to the author's knowledge there have not been any applications of FBG sensors directly on any HTLS conductors.

ACCC® has previously been evaluated for static and fatigue mechanical properties [8], [17]–[20], [29], and dynamic testing of ACCC® was conducted using a newly developed laboratory testing apparatus [30] but none of the existing research on the ACCC® overhead conductor has incorporated the use of FBG sensors to obtain strain data. To further understand the impact response of the conductor under the extreme loading conditions reported in [30], additional lower impact energy dynamic tests were performed in this study with a new measurement approach. The aims were to determine

the capability and sensitivity of FBG sensors to identify the position and magnitude of impact and the dynamic response of the conductors and the load fixture following impact.

4.2 Experimental methods

4.2.1 Sample preparation and FBG data collection

A 1.1 m section of Drake size ACCC® manufactured and donated by CTC Global was prepared and used in this research. The sensor array produced by Technica Optical Components, LLC. consisted of Corning®SMF-28®Optical fiber with an acrylate coating and five FBG sensors naturally packaged with center to center separations of contiguous sensors of 200, 100, 100, and 200 mm along the fiber. In order to extend the useable measurement range of the sensors, the hybrid composite core of the conductor was removed from the outer aluminum strands and tensioned to 13.34 kN in an Instron 5982 Dual Column Floor Frame. The FBG array was then centered on the composite rod and adhered along the surface in the axial direction using West System®G/flex®650 Toughened Epoxy per manufacturer instructions. The epoxy was applied in two coats along the entire gauge length of the composite rod to achieve the sensor locations depicted in Figure 4-2. Strain Data from the FBG sensor array was collected using a Micron Optics si155 Hyperion Optical Sensing Unit having a reported wavelength accuracy and repeatability of 1 pm, equivalent to about 1 $\mu\epsilon$. The accompanying software, Micron Optics ENLIGHT, was used to collect and convert wavelength data to strain.

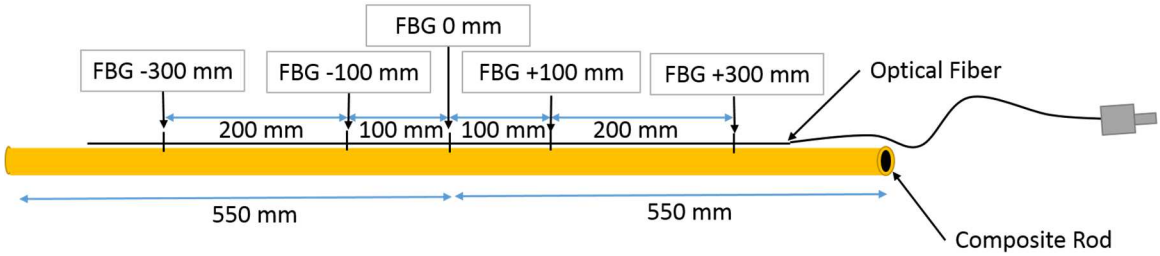

Figure 4-2: Locations of mounted sensors.

4.2.2 Mechanical static testing

Mechanical tests were conducted to evaluate the effect of various simple and multiaxial loads on the response of the FBG sensors. To verify the response of the FBGs to axial loading, the composite rod from the ACCC® conductor with attached sensors and no aluminum strands was tensioned from 0.00 kN to 35.5 kN in the Instron test frame shown in Figure 4-3. Surface strains were recorded independently from the five FBG sensors epoxied to the surface and from an Instron 2630 static clip-on extensometer. Additional axial testing was performed with the sensor mounted rod reinserted into the aluminum stranding to determine the effect of the Al strands on the strain measurements.

Figure 4-3: Tensile testing of ACCC® rod with FBG array mounted to surface.

To show the response of the FBG sensors under a constant bending strain, a single FBG sensor was mounted on the surface in the middle of a 280 mm composite rod section taken from the CTC Global conductor. The rod was then subjected to a proof load of 2.05 kN using the four-point bend test setup developed by Burks and Kumosa [21]. The FBG sensor was positioned on the axial tension side of the rod. Special care was taken to position the sensor directly opposite to the applied load side of the rod to avoid any multiaxial load situations.

To show the effect of combined axial tension and bending loads on the FBG strain measurements, static 3-point bend –axial tension tests on bare CTC Global rods and rods

with Al strands were also performed (Figure 4-4). The tests were performed using the setup already presented in [30]. The responses of the five sensor FBG array mounted to the composite rod with and without aluminum strands were recorded for a 1.0 kN static load applied transversely to the center of the tensioned rod or conductor. The experimental setup in Figure 4-4 consisted of initial boundary conditions of axial tensions from 2.87 to 28.67 kN in increments of 2.87 kN. The same Dillon Mechanical AP Dynamometer was used to measure both the initial and final axial tension after the transverse loading. Again, special care was taken to control the position of the sensors to be 180° offset from the load side of the specimen (rod or conductor). This positioning was relatively easy to accomplish for the bare rod. For the full conductor where the sensors were not visible through the aluminum, best efforts were made to position the sensors at the bottom or the top (maximum bending tension or compression, respectively) and to have the transverse load directly above the center sensor.

Figure 4-4: Tensioned three point bend setup for ACCC® rod and conductor.

4.2.3 Mechanical dynamic testing

For the dynamic tests, the sensors were mounted on the rod as in Section 4.2.1 before reinserting the rod into the aluminum stranding. A pendulum with a 0.45 kg mass was released from various heights to achieve impact energies ranging from 0.01 to 2.25 J , contacting the conductor 180° relative to the sensor array (i.e., on the opposite side as shown in Figure 4-5). An additional larger pendulum of 46.7 kg mass was used to achieve an impact energy of 33.1 J. The experimental boundary conditions for all dynamic tests consisted of fixed conductor ends with initial displacements to create a pre-impact axial tension of 12.45 kN. For each experimental test, the measured strain at each FBG sensor was zeroed prior to impact and recorded for 500 ms prior and 5 s after impact at a sampling rate of 1 kHz. A fast Fourier transform was applied to the time history of strain data to obtain the single-sided frequency content of the signal from each FBG sensor.

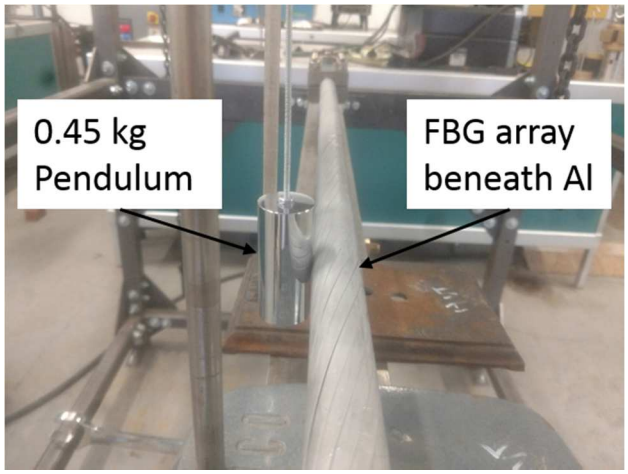

Figure 4-5: Pendulum and mounted conductor for low energy impact tests.

To evaluate the ability of the sensors to identify the point of contact, a 1.48 J impact was imparted at 0., 100, 200, and 300 mm from the center of the conductor, as shown in

Figure 4-6. Data from the five FBG sensor array was recorded for each impact. An additional impact of 33.1 J was also imparted at 0 mm (Impact A) to evaluate the response of the sensors under a significantly higher impact energy.

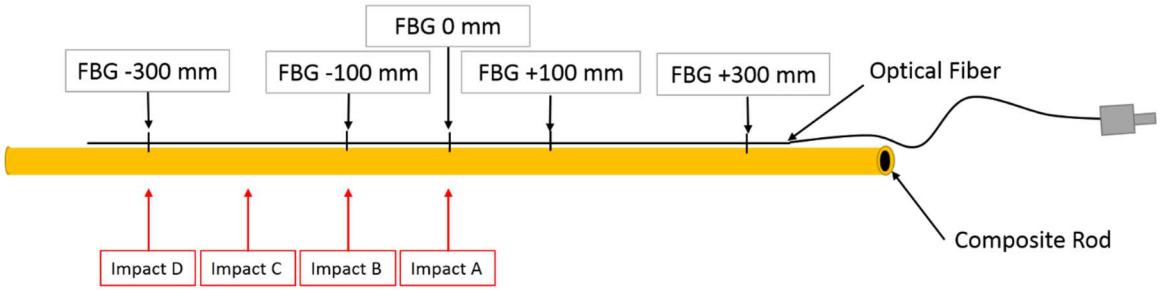

Figure 4-6: Locations of impact relative to FBG sensors.

4.3 Finite element analysis

To evaluate the accuracy of the FBG sensors, finite element (FE) analyses of the static axial, four-point bend, and tensioned three-point bend rod-only experiments were conducted using Abaqus 6.13/Standard. One rod model was developed and subjected to the three different load cases. The model shown in Figure 4-7 consisted of eight node reduced integration hexahedral C3D8R continuum elements in both the glass/epoxy and carbon/epoxy composite sections. The engineering constants for the two orthotropic materials are given in Table 4.1. The hybrid composite rod was modeled to have a 3.37 mm radius of carbon/epoxy and 4.76 mm outer radius of glass/epoxy with a perfectly bonded interface. All FE models of the rod consisted of the same element mesh density in the rod cross-section. The four-point bend model consisted of 600 elements along the 280 mm length, and the tensioned three-point bend and axial models had 600 elements along 890 mm of composite rod.

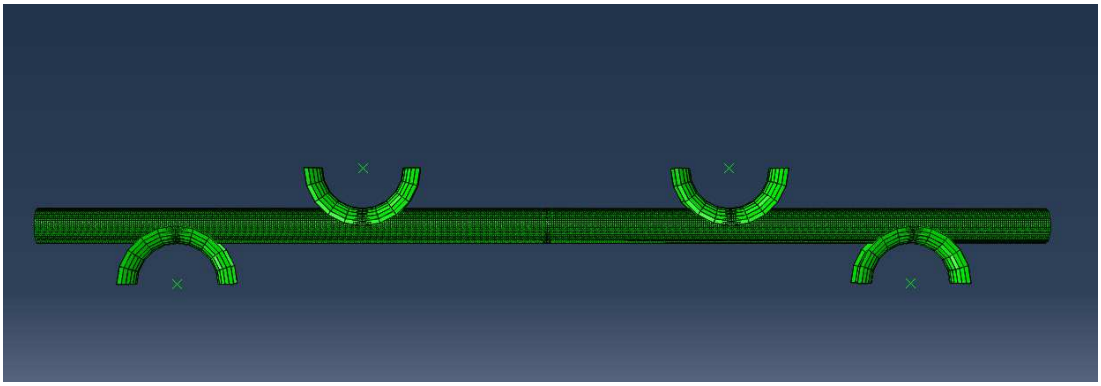

Figure 4-7: FE model of ACCC® with four-point bending boundary conditions.

Table 4.1: Constitutive material properties for ACCC® rod components [43], [47]*.(Note that these values are slightly different than previously used in Chapter 2)*

	Glass/Epoxy Composite	Carbon/Epoxy Composite
$E_1(GPa)$	7.41	5.7
$E_2(GPa)$	7.41	5.7
$E_3(GPa)$	49.3	139.0
ν_{12}	0.408	0.44
ν_{13}	0.038	0.005
ν_{23}	0.038	0.005
$G_{12}(GPa)$	4.12	2.44
$G_{13}(GPa)$	4.80	2.67
$G_{23}(GPa)$	4.80	2.67

4.4 Results and discussion

4.4.1 Static testing

The response of all five FBGs, seen in Figure 4-8a, to axial straining of the rod closely matches that of the Instron extensometer with a measured overall axial Young's modulus from the FBG array, $E_{FBG} = 99.9\ GPa$ and standard deviation between the five sensors of σ = 0.36 GPa. Readings from the Instron extensometer produced an elastic modulus of $E_{ext} = 97.98\ GPa$, differing from the FBGs by 1.94%. Figure 4-8b shows the static three-point bend tensile strains of a tensioned rod with no aluminum subjected to a 1.0 kN transverse load. As expected, with increasing axial tensions the strains

induced from the application of a 1.0 kN transverse load decreased. Strains were also highest in the center as is expected for a three-point bend test.

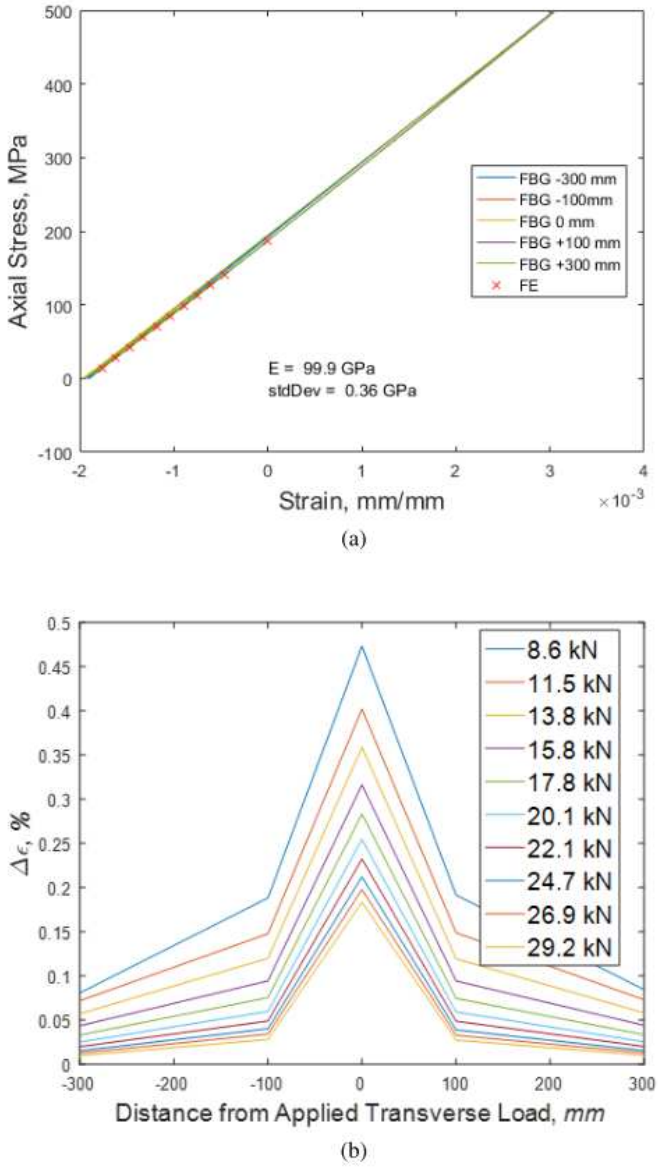

Figure 4-8: Static response of FBG sensors to A) axial loading, and B) tensioned 3-point bend. Legend in B indicates final axial tension after transverse loading. Tests are for bare ACCC® rod.

Figure 4-9, shows the change in the measured strains of the FBG sensors upon application of the 1.0 kN transverse force for the initial tensions of 2.87, 14.3, and 28.7 kN. The loads in the legend of the figures are the final measured axial tensions after

application of the transverse load. As expected, with increasing axial tension there is less deflection on the tensile side of the rod corresponding to the decreasing strains in Figure 4-9a. In Figure 4-9b, it is evident that application of the 1.0 kN transverse load causes an additional amount of axial tensile strain sufficient to negate any accompanied compressive strain at the ends of the composite rod due to bending. This is especially true for low initial axial tensions such as 2.87 kN.

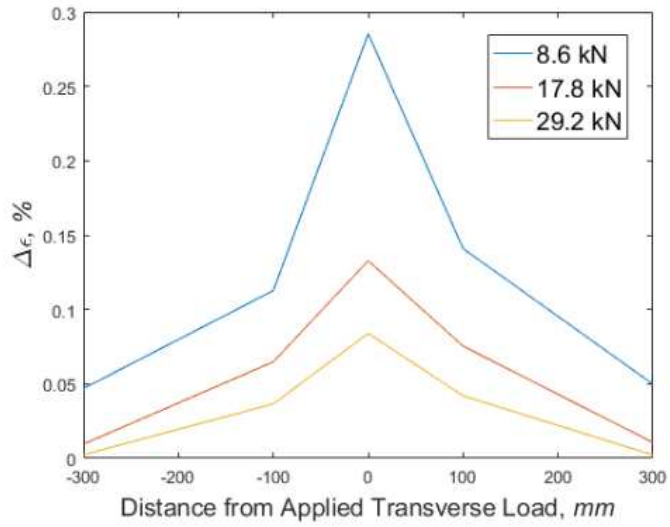

(a)

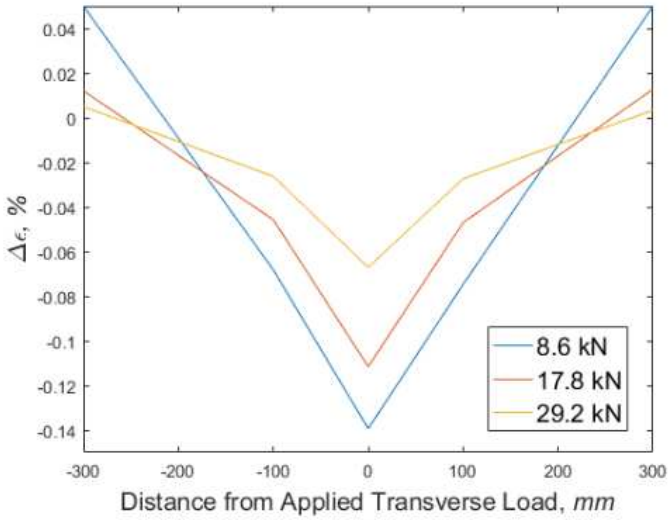

(b)

Figure 4-9: FBG strains for a) tension, and b) compression sides of ACCC® rod surrounded by aluminum strands under different final measured axial tensions.

Experimental and numerical results of the measured rod strains under axial tension agree well as shown in Figure 4-10. The model with simple boundary conditions demonstrates that the axial properties of the composites are accurate. The ability of the FBG sensors to accurately measure axial strain was already confirmed by comparison to the extensometer.

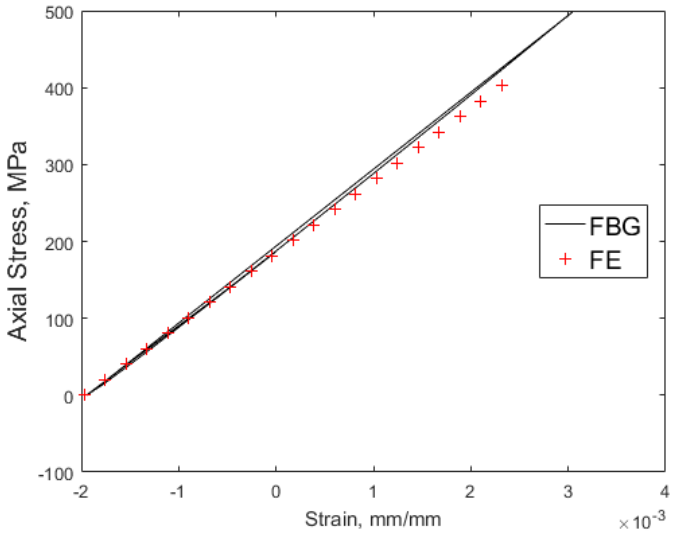

Figure 4-10: Experimental and numerical strains of composite rod subjected to axial loading.

The experimental and numerical four-point bend evaluations shown in Figure 4-11 were conducted to demonstrate that the sensors could accurately measure strains due to pure bending. The experimental results agreed well with the numerical results as shown in Figure 4-12. This suggests that along with the axial material properties, the flexure properties of the model are appropriate and the FBG measurements are not impacted by the bending of the optical fiber. After demonstrating the accuracy of the FBG sensors in single mode loading, the more complex combined loading case of tensioned three-point bending was modeled. As the boundary conditions became multi-axial with both tension and transverse loading, the numerical simulation of tensioned three-point bending of the composite rod generally followed the results of the experiment as seen in Figure 4-13, with some limitations. At the ends of the conductor, bending strains were much less significant and the model closely matched the experimental result for the predominantly axial loading. However, at the center sensor which experienced the largest effect of combined loading, the differences were more significant. Possible sources of this

discrepancy include a potential strain gradient across the 7.0 mm sensor grating length due to the nature of a tensioned three-point bend test, a misalignment of the sensors in either or both the rotational direction (i.e., not 180° offset from the load) and the axial direction (i.e., the center sensor not directly below the load). It is also possible that the complex boundary conditions of the tensioned three-point bending are not fully reflected in the FE model. In addition, comparisons of strains were made between the composite rod with no aluminum and the entire conductor with aluminum under axial loading (Figure 4-14) and under both axial and transverse loads (Figure 4-15). It is clear that the aluminum surrounding the core reduces the strains under the same loading conditions. The aluminum, while less stiff than the hybrid composite rod, has a 14.0 mm outer radius and much more material than the rod. The aluminum carries a significant portion of the axial and bending loads, leading to decreased stresses on the composite rod under the same loading conditions. Thus, the total axial and bending strains of the rod are reduced, but still measured effectively by the FBG sensors.

Due to the symmetry used in the FE analysis for the rod, the resulting strains are mirrored about the center of the conductor. In the experimental results of axial strain along the rod as seen in Figure 4-8b, Figure 4-9, and Figure 4-13, axial misalignments contribute to variations in strain at the assumed locations of the FBG sensors. This non-symmetry in the experiment is most evident in the case of the entire conductor as seen in Figure 4-15 where it was the most difficult to properly position the load relative to the sensors.

(a)

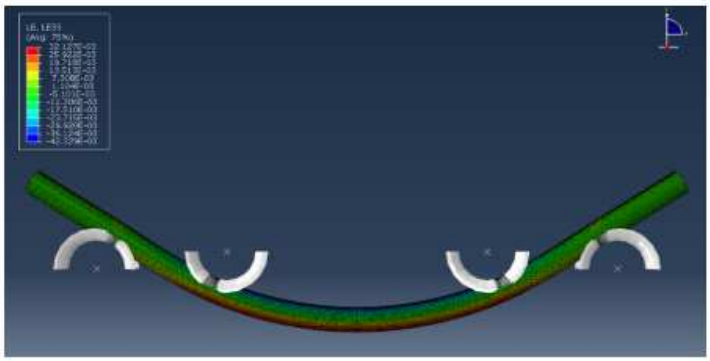

(b)

Figure 4-11: Experimental and numerical four-point loading of bare rod.

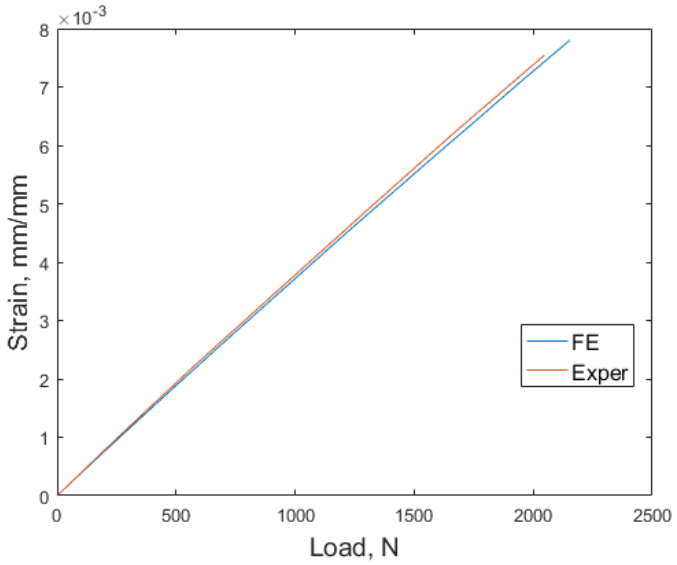

Figure 4-12: Experimental and numerical results of four-point bend strains.

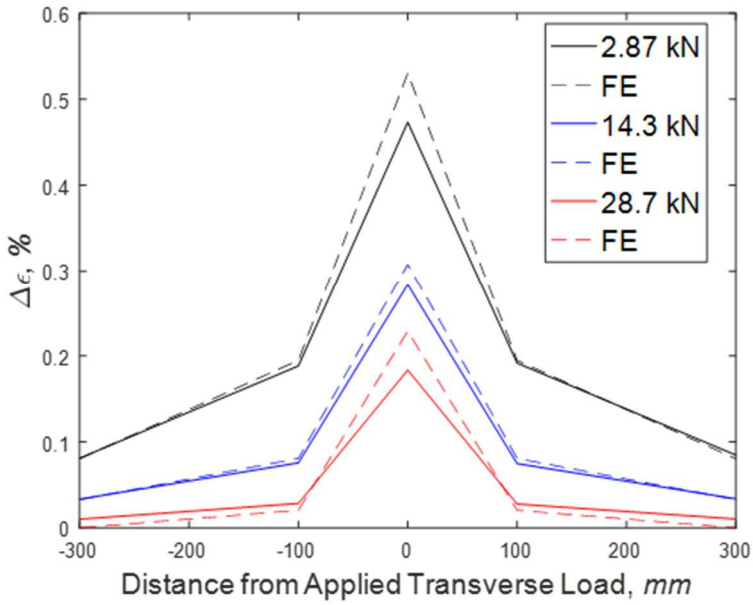

Figure 4-13: Experimental and numerical strains of composite rod subjected to 1.0 kN transverse load.

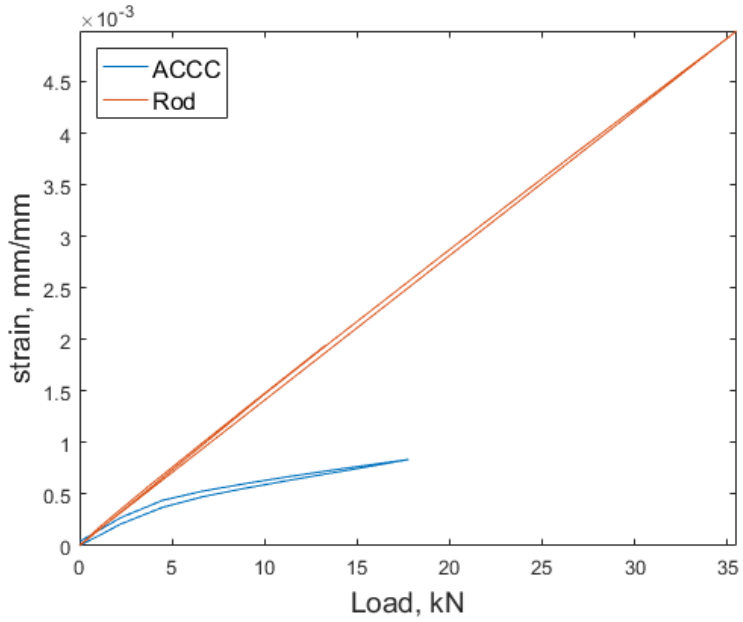

Figure 4-14: FBG strains of ACCC® rod subjected to axial tension, with and without aluminum stranding.

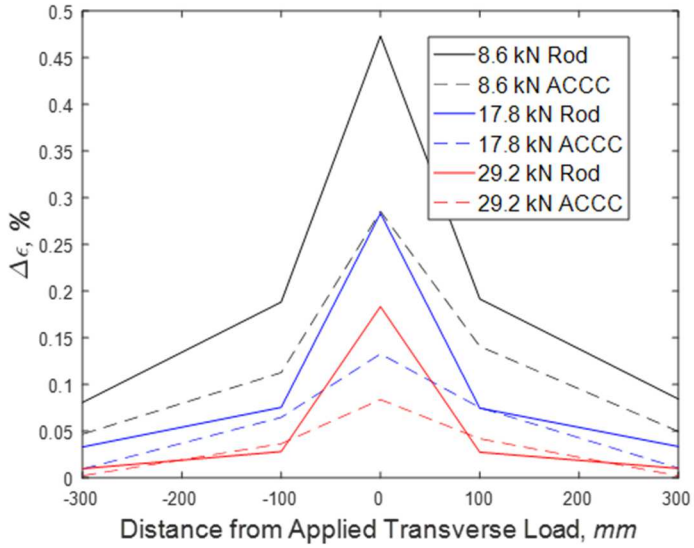

Figure 4-15: FBG strains of composite rod subjected to three-point bending, with and without aluminum stranding.

4.4.2 Dynamic testing

4.4.2.1 Sensitivity

The responses from the five FBG sensors in the time and frequency domains when exposed to the three impact energies at the center of the conductor (position C in Figure 4-6) are shown in Figure 4-16, Figure 4-17, and Figure 4-18. The lowest energy impact produced an increase of approximately 30 με at the center of the conductor at the moment of impact. Such small amplitudes, however, are quickly dissipated by damping in the system. The higher energy impacts, as seen in Figure 4-17 and Figure 4-18, clearly produce both a transient and steady state response in the time domain, with higher strain amplitudes from the higher impact energies. The frequency content of each of the three energies are similar with all five FBG signals having two prominent peaks. The first of these peaks, at approximately 22.5 Hz, corresponds to the dominant frequency of the steady state response of the system and is clearly visible in the time domain response when all five FBGs oscillate in phase about the equilibrium value of 0 με. Figure 4-19

illustrates the time and frequency of the response between 0.5 s and 1.5 s after impact (1.0−2.0s after the start of the recording). The reduced peak at approximately 26 Hz represents the transient response of the conductor which is damped more quickly than the steady state frequency. Both the steady state and transient frequencies would be expected to change with different initial tensions, sample lengths, and many other factors.

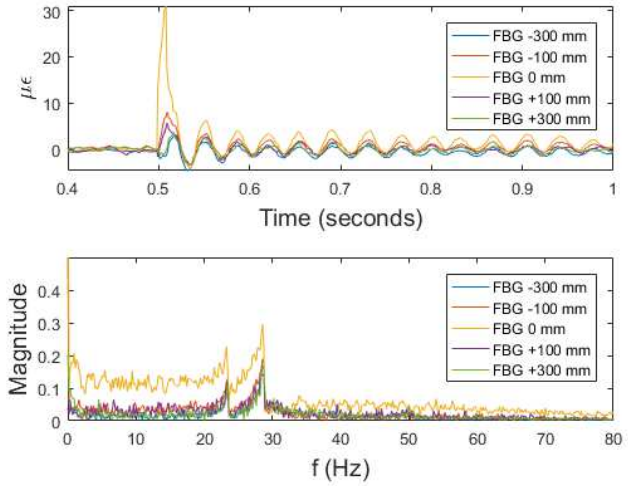

Figure 4-16: Sensitivity plots for impacting energies of 11.3E − 3 J.

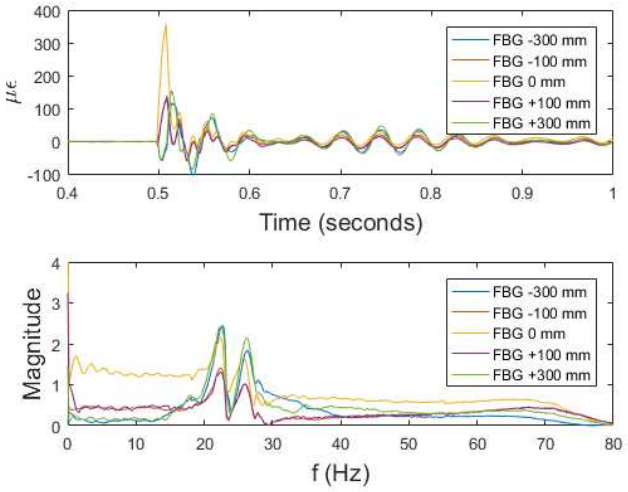

Figure 4-17: Sensitivity plots for impacting energies of 1.48 J.

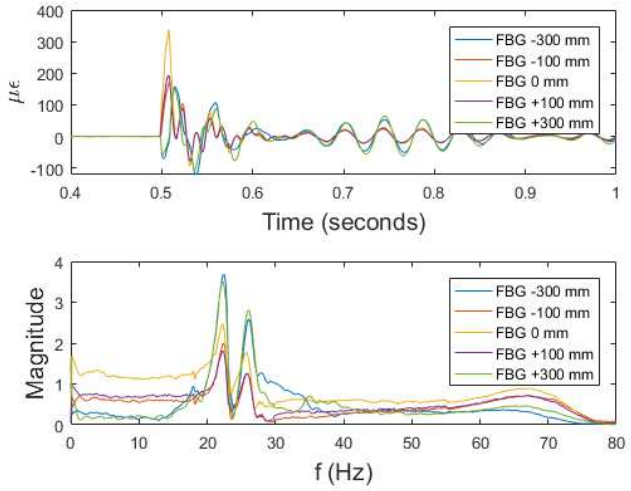

Figure 4-18: Sensitivity plots for impacting energies of 2.25 J.

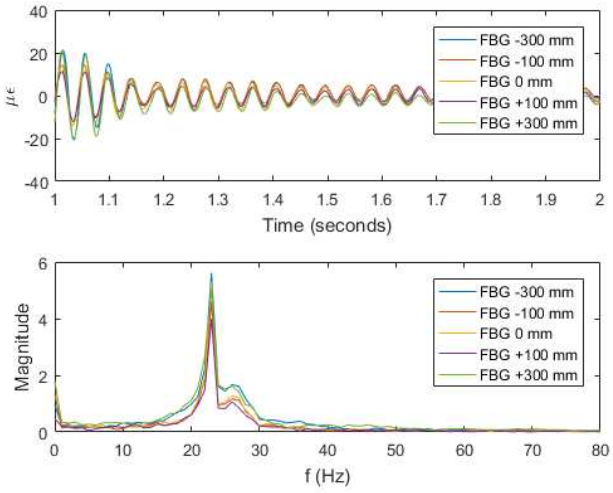

Figure 4-19: Steady state response of conductor subjected to 2.25 J center impact.

4.4.2.2 Position determination

The conductor response to a center impact is presented in Figure 4-20a. The strain measured by the center sensor was the largest as the conductor exhibited the most bending at the location of the impact. This maximum strain at the point of the impact is also demonstrated in Figure 4-20b and Figure 4-20d where the location of the impact coincided with an FBG sensor. In Figure 4-20c, impact occurred halfway between the

two sensors that measured the greatest and approximately equal amplitudes of strain, suggesting that an impact location can still be determined even if it does not coincide with the position of a sensor. In addition, Figure 4-21 shows the frequency response of the sensor arrays to the four different position impacts. The frequency component magnitudes are all very similar with two dominant peaks between 20 and 30 Hz, much the same as for the center impacts of various energies in Figure 4-16, Figure 4-17, and Figure 4-18.

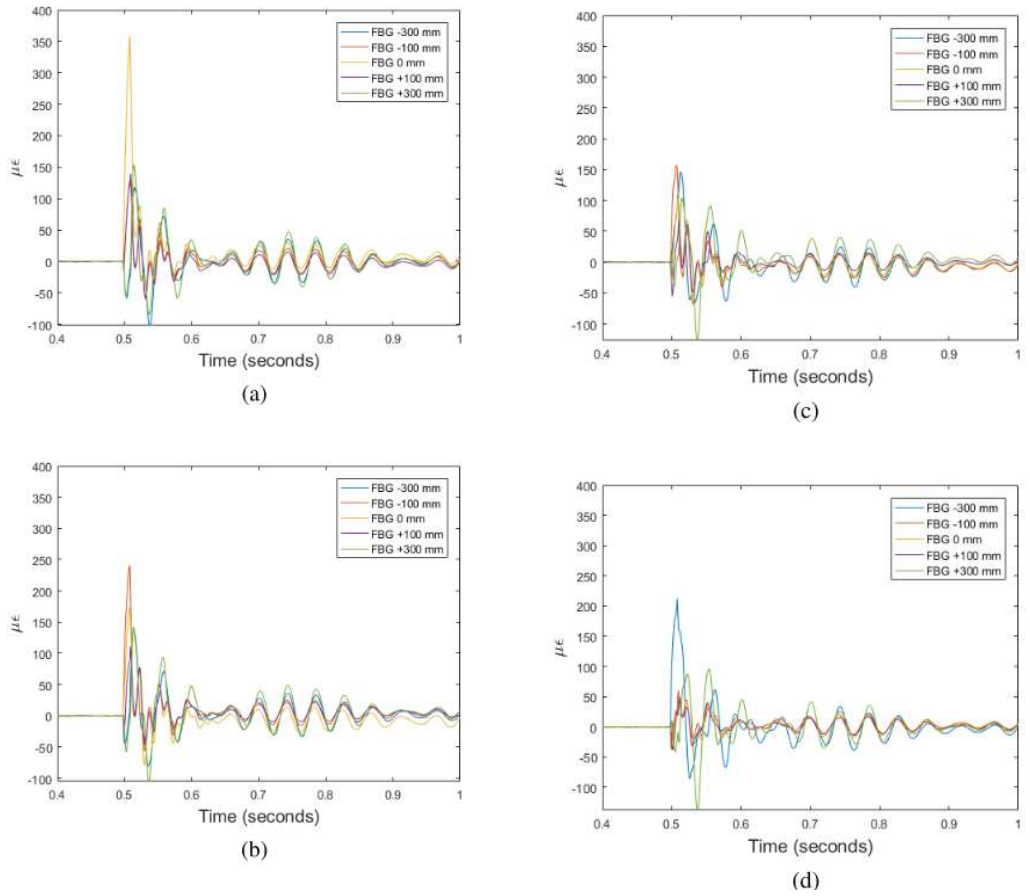

Figure 4-20: Strain response of 1.48 J impact at a) 0 mm, b) 100 mm, c) 200 mm, d) 300 mm from the conductor center.

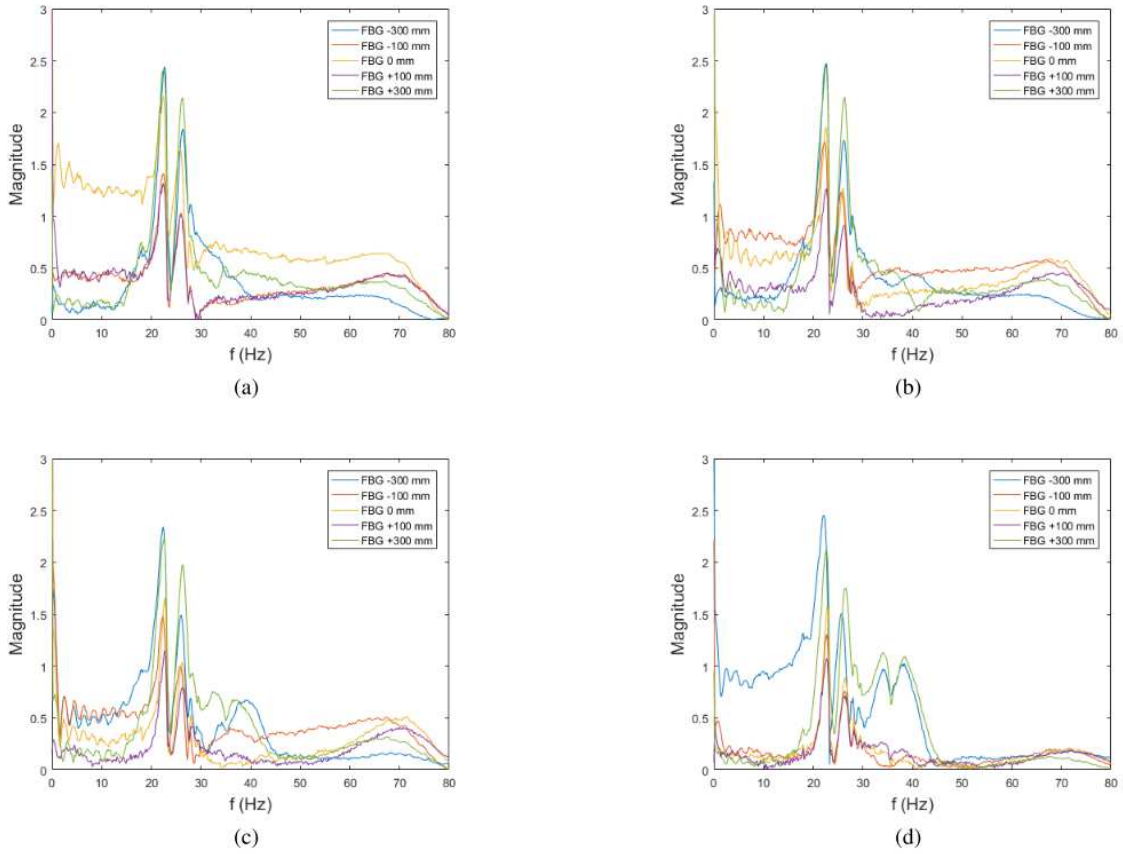

Figure 4-21: Frequency content of 1.48 J impact at a) 0 mm, b) 100 mm, c) 200 mm, d) 300 mm from the conductor center.

Even at a higher impact energy of 33.1 J using a larger pendulum, impact location can still be accurately identified as shown in Figure 4-22. The largest strain occurred at the point of impact and the pairs of sensors equidistant from the impact showed very similar initial strain values. The frequency domain plot in Figure 4-22 includes a significant low frequency response. The pendulum remained in contact with the conductor during the initial impact and thus the low frequency content could be a result of the conductor interacting with the mass of the pendulum and the test fixture. When the first half-second after impact is removed as in Figure 4-23, the familiar transient and steady state

frequencies are much more dominant. Due to the higher impact energy, the transient frequency is still significant after one half-second.

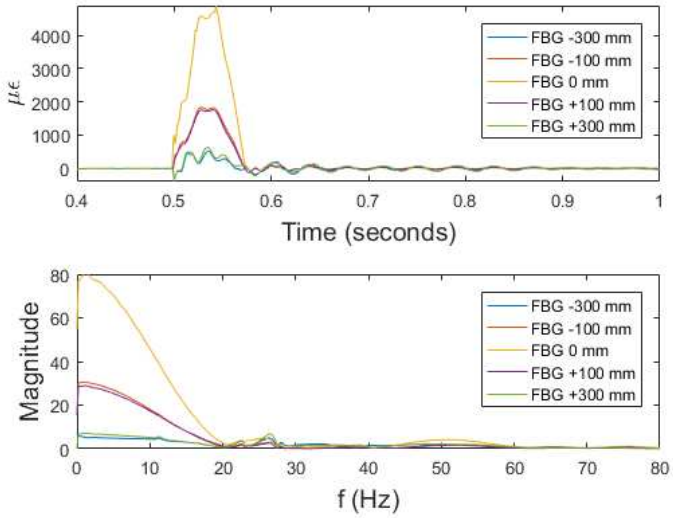

Figure 4-22: Strain response and frequency content for 33.1 J impact.

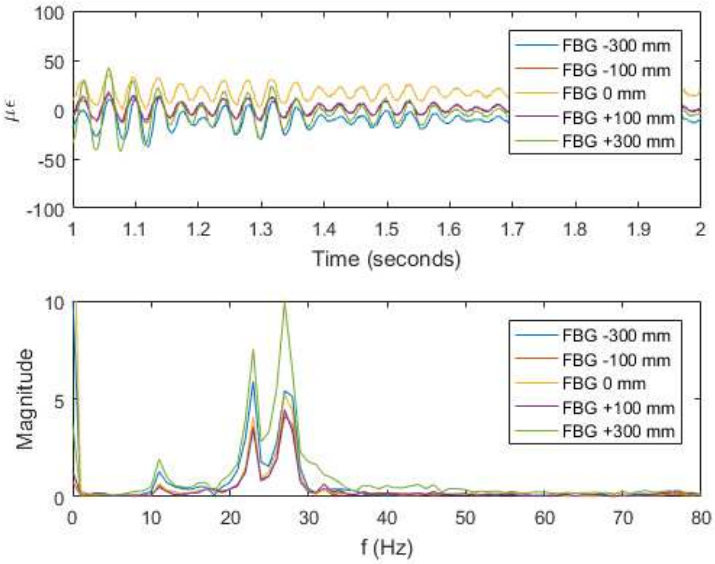

Figure 4-23: Steady state strain response and frequency content for 33.1 J impact.

4.4.3 Explanation of modeling errors encountered in Chapter 2 [30]

In Figure 4-16, Figure 4-17, Figure 4-18, Figure 4-20, and Figure 4-22 the time history of strain data shows complex dynamic responses of the ACCC® conductor to low-velocity impacts. This is evident as the sensor measurements closest to the point of impact initially increase with tensile strain, whereas the sensors at certain distances from the impact show compressive strains. This presence of tensile and compressive strains on the same side of the conductor immediately following impact indicates the conductor exhibits a more complicated deformation type than the catenary curve of a tensioned hanging cable. The significant dynamic response observed along the conductor explains why the simplistic FE model developed in previous work [30] generated large errors in the dynamic response of the conductor under extreme impact comparisons. In the boundary conditions used in that work and depicted in Figure 2-5, the use of straight one-dimensional elastic beams to reduce the computational cost of the analysis did not provide an accurate dynamic response. As indicated in Chapter 2 [30] a more accurate solution would require a full scale dynamic model of the conductors under impact, or an application of higher order isoparametric beam elements for the reduced model of Figure 2-5.

4.5 Chapter conclusions

This work significantly expands the capabilities already presented in [30] for the impact testing of novel High-Temperature Low-Sag (HTLS) overhead conductors employing a polymer matrix composite core. In particular, this research shows that FBG sensors can effectively monitor one type of HTLS conductor by accurately measuring strains due to static and impact loads. To verify the applicability of the sensors in the

mechanical testing of the conductors, static axial, bending and combined tension-bending load cases were first considered both for bare conductor rods and complete conductors. Very good agreements were obtained between the experimental FBG measured strains and their numerical predictions. Subsequently, impacts tests were performed to evaluate the capabilities of the FBG sensors to monitor dynamic loads and to identify and localize dynamic situations ranging from very small to large impacts. On a 1.1 m long conductor span the sensors allowed detection of impacts as small as 0.01 J. Steady-state and transient responses of the conductor after impact were also identified. Through this research, we have advanced the ongoing discussion regarding structural health monitoring of next generation conductors subjected to impact loads either during installation or in- service.

5 Monitoring mechanical loads in pultruded hybrid composite rods using embedded FBG sensors

Embedding acrylate coated FBG sensors in pultruded composites has seen little attention paid to the quality of measurements made. The thermal limitations of the acrylate buffer have been blamed for causing poor mechanical interface in a pultruded host material. This section of the thesis presents preliminary experimental measurements made using embedded acrylate buffered FBGs and external extensometers. Discrepancies observed between the two types of measurements are discussed and attributed to mechanisms associated with the acrylate buffer interface. Finally, assuming the strain transfer limitations associated with the buffer can be addressed, the optimal placement of embedded optical fibers is discussed based on the limitations of the composite structure and mechanical strength considerations of optical fibers.

5.1 Introduction

Previous work by Waters et al. showed that Fiber Bragg Grating (FBG) sensors mounted to the surface of pultruded hybrid PMC rods provide accurate and repeatable measurements of static strains when compared to finite element and experimental analyses[31], [69]. Kalamkarov et al. investigated the suitability of polyimide coated fiber optic FBG sensors embedded in pultruded fiber reinforced polymer composites for measuring static and dynamic strains [70]–[75]. Acrylate buffered fibers were excluded from his studies after claiming the polymer would not survive the pultrusion process

temperatures [73]. Additional work supports that well bonded bare optical fibers provide superior strain transfer from the host material when compared to buffered fibers; however, handling of fibers in this state is impractical due to their susceptibility to damage [76], [77]. The capabilities and reliability of acrylate buffered optical fibers with FBGs embedded in pultruded composites, especially within power transmission composite structures such as ACCC® have yet to be addressed.

5.2 Effect of FBG fiber location on their survivability in ACCC® cores subject to bending and tension loads

Based on the tensile strength of Corning® SMF28e+® and assuming a perfectly bonded interface between the host material and the optical fiber (most conservative estimate), the optimal location in a Drake sized core (Figure 5-1) when subjected to bending and/or tensile loads can be assessed.

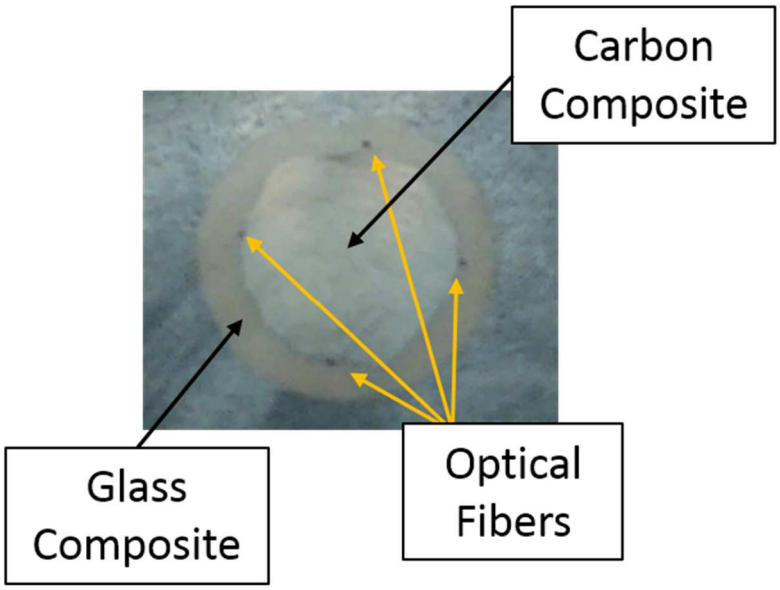

Figure 5-1: Optical fiber arrays embedded in mounted and polished cross-section of pultruded PMC rod

Extending the work performed in Chapter 3 [78] on the combined effects of tension and bending, a simple analytic solution based on superposition for the axial strain can be

expressed by equation 5.1, given the radial location, y, axial load, P, bending radius, R, elastic modulus, E_1=97.4 GPa , and nominal cross sectional area, A = 71.3 mm^2 . The accuracy of equation 5.1 was evaluated in Chapter 3 [78] by performing linear elastic large deformation Finite Element Analyses (FEA) of the ACCC® core subjected to both bending and tension. The rod geometry was wrapped around rigid mandrels having a range of diameters while simultaneously applying several axial tensile loads. The numerical results obtained from the FEA in [78] are presented as a contour plot of axial strain at the carbon/glass interface (y=6.74 mm) subjected to combined bending and tension. The contour data is given only at this location as it was determined to be the most probable initiation site of damage in the structure. Despite being more comprehensive by accounting for nonlinear geometry effects, the numerical model had only a small difference when compared to equation 5.1.

Figure 5-2 gives the expected internal axial strain that would be imposed on an optical fiber residing inside a Drake ACCC® composite core at the interface. The carbon compressive failure and glass compressive failure lines show the loading conditions to initiate compressive damage in the carbon and glass sections, respectively. These lines, along with the carbon tensile failure line provide the limiting bounds for the composite structure.

$$\epsilon_1 = \left(\frac{y}{R} + \frac{P}{E_1 A}\right) \tag{5.1}$$

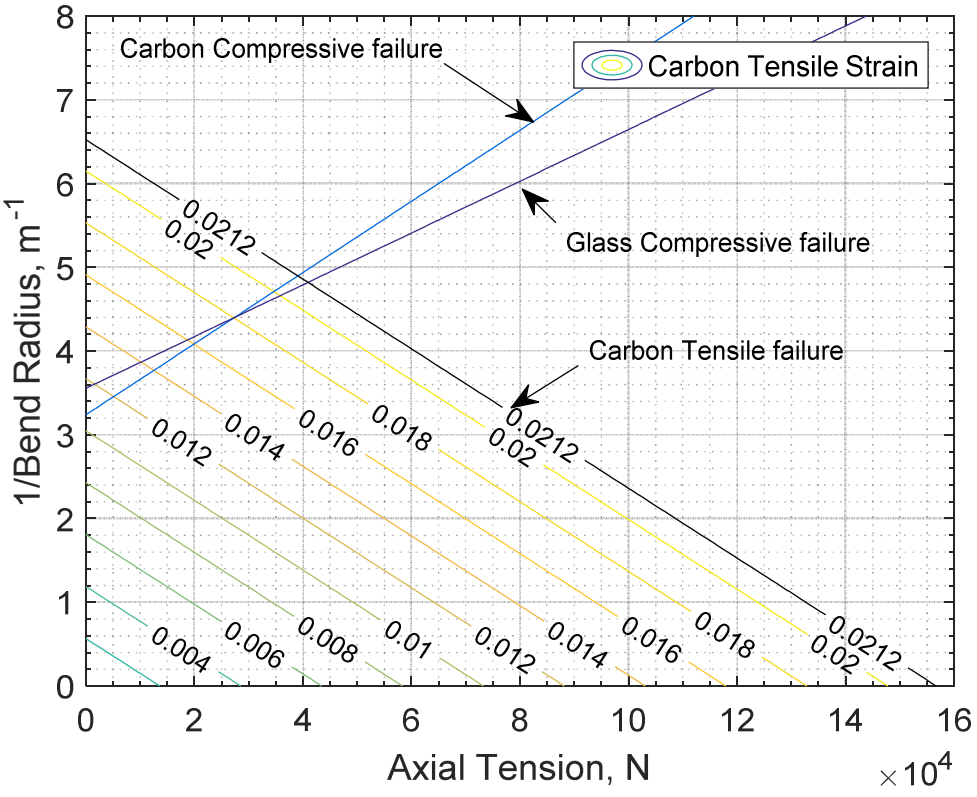

Figure 5-2: Carbon tensile strains at interface with structural damage initiation loading scenarios from chapter 3 and [78]. *Parallel lines indicate the expected maximum internal axial strain at the carbon/glass interface for combined loading scenarios.*

Standard SMF-28e+® is subjected to a proof load of 690 MPa (100 kpsi) which corresponds to 0.98% strain. Yet the probability of a flaw that would lead to failure at a specific strain higher than the proof strain in modern optical fibers is very dependent on the length and Weibull modulus. Using the Weibull modulus and other parameters determined in [79], if the optical fiber tensile failure strain is assumed to be the tensile failure strain of the carbon composite used by Waters et al [78] in Figure 5-2 ($\epsilon = 0.0212$), the probability of failure in a 1 km length is approximately 0.3%, but over a 100 m span is only 0.09% [79]. In service, it is unlikely that 1 km of conductor would exhibit a constant bend radius; however, during installation the conductor must be pulled over

installation pulleys that expose the entire length to bending with additional tensile loads. During transportation and storage, ACCC® conductors are shipped and stored on mandrels that apply bending loads to the length of the conductor. Total conductor length is therefore an important factor to consider when embedding optical fibers in ACCC® composite cores.

For an optical fiber not intended to measure bending strains, a position at the center of the composite structure provides the most resistance to the effects of bending. At this location, the expected strains in the composite can be calculated from the axial tension on the x-axis of Figure 5-2. Up to the typical service loads of 40 kN, a 388 MPa (56.3 kpsi) proof fiber would provide for 100% reliability while a standard 690 MPa (100 kpsi) proof fiber would provide the same reliability up to 71.76 kN.

If instead, a 1380MPa (200 kpsi) proof test fiber is used in the carbon composite region, the failure probability would be reduced significantly since the composite failure strain (2.12%) is much closer to the optical fiber proof strain, (1.96%). For guaranteed survivability in this region, a 1491 MPa (216.2kpsi) proofed fiber is required to match the tensile strength of the composite structure.

If the optical fiber is intended to measure strains within the structure as suggested by Hoffman et al for shape sensing applications [68], a central location would not provide sensitivity to the bending induced strains. Improved sensitivity can be achieved with an increased radial distance from the center, but this requires a higher proofed fiber to maintain a guaranteed survivability.

Rearranging equation 5.1 and using Figure 5-2 to determine the minimum bend radius, the optimal radial location to guarantee survivability of a given proofed optical

fiber inside the carbon composite section can be determined for a given axial load and proof stress fiber. Below the axial load of 41.1 kN the expected compressive failure conditions (carbon compressive or glass compressive failure) should be considered in determining the maximum bending curvature. Above 41.1 kN, the maximum bending curvature must be determined from the carbon tensile failure line.

Even for long spans of ACCC® strung at the maximum recommended 35% of the rated tensile strength, or 64 kN [80], the uniform axial strain begins at 0.88% and the addition of bending strains would require a 1380MPa (200 kpsi) proof fiber be placed no more than 2.69 mm away from the center. This would not exceed the minimum proof strength considering the damage initiating limits from Figure 5-2 and equation 5.1. In contrast, a 690 MPa (100 kpsi) proof fiber would require a radial location of r = 0.152 mm.

5.3 Methods

5.3.1 Experimental

5.3.1.1 Specimen preparation and data collection

Dual acrylate coated Corning® SMF-28e+® Optical fibers containing naturally packaged FBGs having gauge lengths of 7 mm were produced by Technica Optical Components, LLC. and embedded by CTC Global into a pultruded hybrid PMC rod. The standard dual acrylate buffer consists of a primary (innermost) and secondary (outer) coating to protect the optical fiber. The optical fibers indicated in Figure 5-1 were nominally located at the interface of the glass and carbon sections of the composite in four quadrants. The radial placement was chosen for being the most probable location for damage to initiate in a rod subjected to pure bending[17], [18], [78]. Despite the

successful production of several specimens containing FBG sensors, only one was made available by the manufacturer for this research. Therefore, the experimental work was conducted in a manner to maximize the number of experiments before permanent damage to the 1066 mm long sample was created. In related work, not addressed in this research a residual optical fiber manufacturing strain of 0.1% was measured using FBGs in a 30.6 m long section of pultruded composite core after cooling.

Strain data from the FBG sensor arrays was collected using a Micron Optics si155 Hyperion Optical Sensing Unit having a reported wavelength accuracy and repeatability of 1 pm, equivalent to about 1 με. The accompanying software, Micron Optics ENLIGHT, was used to collect and convert wavelength data to strains using equation 5.2, where the opto-elastic coefficient K is 0.78, λ is the measured peak wavelength during the experiment, and λ_0 is the initial FBG peak wavelength. Temperatures were assumed constant for all experiments.

$$\epsilon = \frac{1}{K}\left(\frac{\Delta\lambda}{\lambda_0}\right) \tag{5.2}$$

5.3.1.2 Four-point bending

Four-point bend was imposed using a test fixture having a support span of 203.2 mm and a load to span ratio of ½ [31]. The specimen was positioned in the test fixture such that two opposing FBG containing optical fibers were located at the maximum and minimum bending strain positions. An extension rate of 5.0 mm/min was applied to reach a flexure proof load of 1.5 kN, 33% of the Flexure Strength (FS) previously determined using the same setup [10], [29]. This proof load was chosen to minimize the risk of

damaging the single specimen as ACCC® cores subjected to pure bending are known to exhibit sudden structural failure without noticeable warning[17], [18], [21], [30], [78].

Three tests were performed with the load immediately removed upon reaching the proof load to determine the repeatability of the measurements from the embedded sensor subjected to multiple loading cycles. Subsequently, to evaluate the long term stability of the embedded FBG sensors, the same specimen was subjected to a single relaxation/creep test were the flexural extension was held for 1.5 minutes upon reaching the proof load. Applied flexural load and crosshead displacement were recorded for the duration of the experiments.

5.3.1.3 Uniaxial tension

Following flexural testing, the specimen was reduced in length by 254 mm and subjected to three uniaxial tensile tests in an attempt to identify any limitations of the embedded sensor to static tensile loads. After length reduction, only one FBG sensor remained in the specimen and on an optical fiber different than the ones used in the bending tests. During the bending tests the remaining sensor would have been exposed to negligible strains since it was nominally located at the neutral bending plane of the specimen. Using an Instron 5982 Dual Column load frame the tensile specimen was held in termination collets commercially available from CTC. At an extension rate of 5.0 mm/min, the 222 mm gauge length of the specimen was initially loaded to 20 kN with an immediate unload. Two tensile relaxation tests followed with extension holds at 20 kN and 30 kN, respectively. In the relaxation tests, data collection was stopped when a viscoelastic response of the specimen was no longer observed. The applied load measured with a 100 kN load cell, and strain measured by the surface mounted clip-on

extensometer were recorded using a computer running Bluehill®3 separate from the FBG measurement software.

5.3.2 Numerical

To better quantify the expected axial strains along the embedded FBG optical fibers, finite element (FE) analyses of the static uni-axial and four-point bending experiments were conducted using Abaqus 2017/Standard. One model of the composite rod was developed and subjected to the different load cases. The model shown in Figure 5-3 consisted of eight node reduced integration hexahedral C3D8R continuum elements in both the glass/epoxy and carbon/epoxy composite sections. The engineering constants used for the two orthotropic materials are given in Table 5.1 [78]. The hybrid composite rod was modeled to have a 3.37 mm radius of carbon/epoxy and 4.76 mm outer radius of glass/epoxy with a perfectly bonded interface. The model consisted of 600 elements along the 280 mm axial length.

Table 5.1: Elastic constants for composite constituents [78].

	Glass/Epoxy Composite	Carbon/Epoxy Composite
E1(GPa)	49.3	159.6
E2(GPa),E3(GPa)	9.27	7.37
v12, v13	0.052	0.012
v23	0.545	0.478
G12(GPa),G13(GPa)	5.25	3.97
G23(GPa)	4.74	3.12

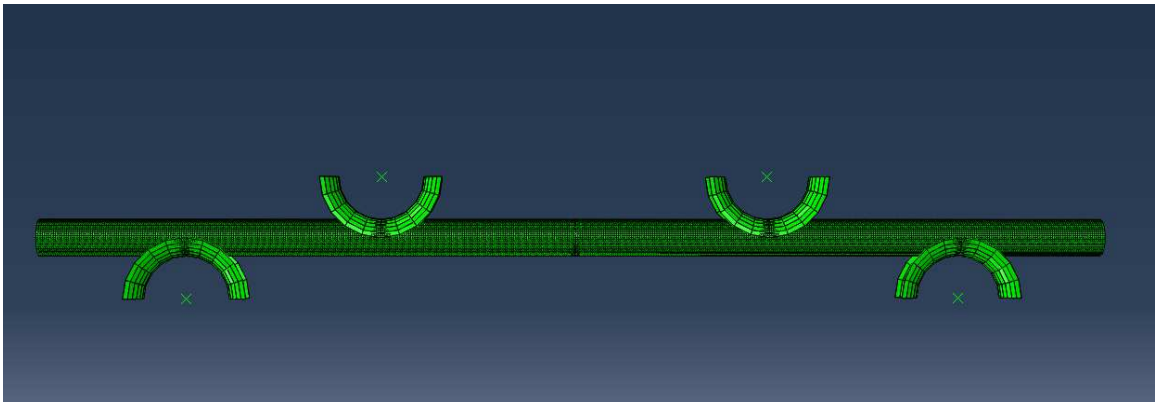

Figure 5-3: FE model of hybrid composite rod subjected to four-point bending.

5.4 Results and Discussion

5.4.1 Four-point bending

The experimentally measured response shown in Figure 5-4 to four-point flexure shows reasonable agreement with the numerical finite element model after toe compensation to account for the specimen settling in the loading pins. The repeatability of the structure's load and displacement response in the three tests suggests that no structural damage was generated. Additionally, the numerical results are shown to correlate well with the experimentally measured values.

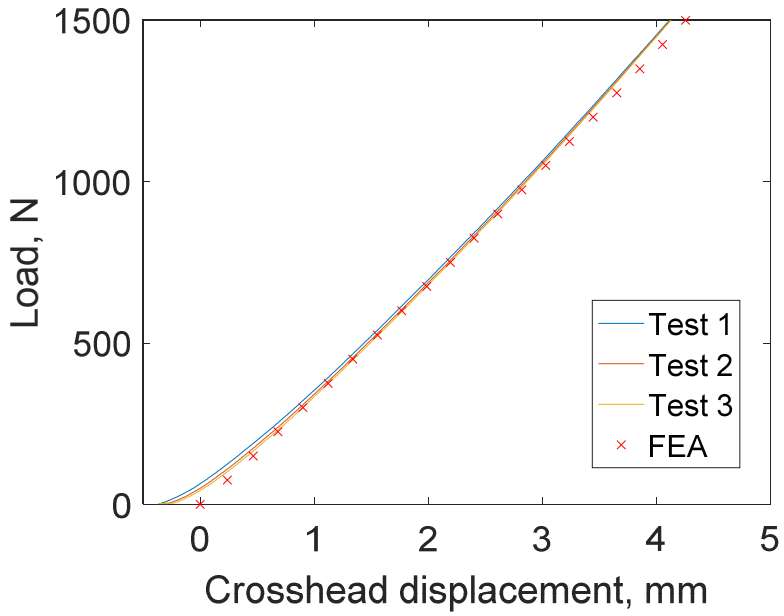

Figure 5-4:Experimental and numerical four-point response.

The mean internal bending strains indicated by the embedded FBG sensors of the sample subjected to the 1.5 kN flexural proof are shown with the numerically determined axial strain profile at the carbon/glass interface as it relates to the center of the four-point fixture in Figure 5-5. In four-point bending, the maximum strain imparted to the embedded optical fiber is expected to be constant in the 101.6 mm region of maximum bending between the loading pins. Outside the maximum bending region, the magnitude of the axial strain reduces linearly to zero in the 50.8 mm section from the load pin to the support pin. The observed local peaks in the FEA model around 50 mm and 100 mm are caused by the complex strain fields imposed by contact with the load and support pins. These artifacts are assumed to have a negligible influence on the measurements of the embedded FBG sensors, which are located closer to the center of the specimen. The mean tensile and compressive FBG indicated strains are found to differ from the FEA values by 4.5% and 4.8%, respectively.

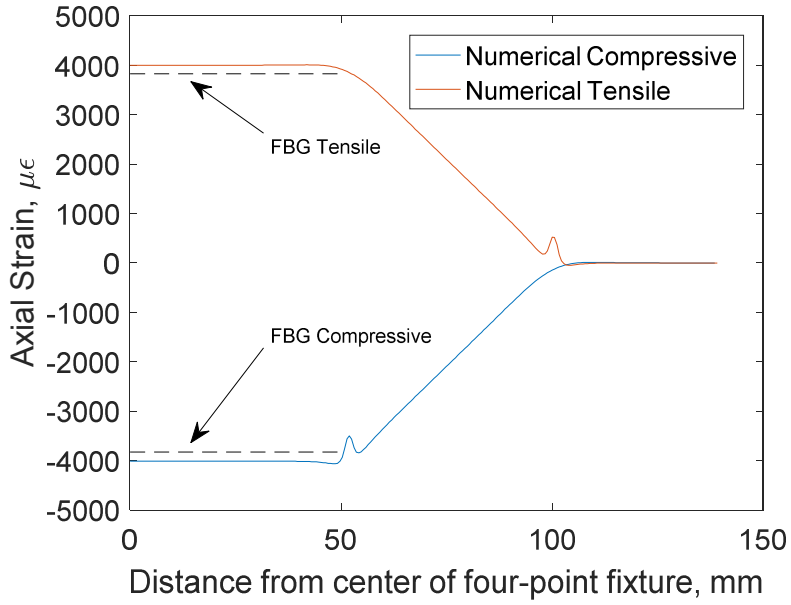

Figure 5-5: Numerical distribution of bending strains at nominal interface of carbon and glass regions in four-point bend fixture.

Since damage to the composite structure or embedded optical sensors was not observed, the flexural hold test was performed to simulate the condition of an ACCC® conductor wrapped on a storage drum (diameter of 1.365 m). The flexure proof load of 1.5 kN corresponds to a bending diameter of 1.67 m, nearly three times larger than the diameter that Burks determined to initiate bending damage using acoustic emissions[18].

Upon reaching the flexure hold in Figure 5-6, the indicated tensile and compressive bending strains are 3811 με and -3820 με, respectively. At the end of the 87.6 s of maintained flexion in Figure 5-6, the magnitude of indicated strain from the compressive bend region decreased by 1.649 %, while the indicated tensile strain experienced a 0.446% reduction. The difference observed in the bending strain relaxations could be caused by natural variations within the composite. Ultimately, the time of 87.6 s is more representative of conditions that might occur during installation when the conductor passes over several installation pulleys during the stringing process. Simulation of

conductor storage on a drum would be better represented by longer hold times where the creep behavior of the FBG sensors could be evaluated.

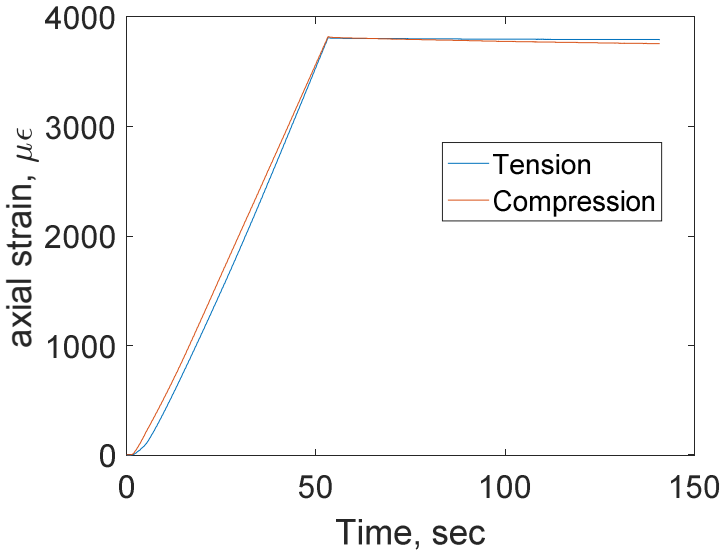

Figure 5-6: Experimental four-point bend with extension hold at 1.5 kN.

5.4.2 Uniaxial tension

In uniaxial tension up to 20 kN, there is reasonable agreement between the surface mounted Instron extensometer, the single FBG sensor nominally embedded at the glass/carbon interface, and the non-linear FE analysis as seen in Figure 5-7. The average elastic response determined from the slopes of the stress-strain curve for the specimen from the uniaxial proof load cycles is given in Table 5.2.

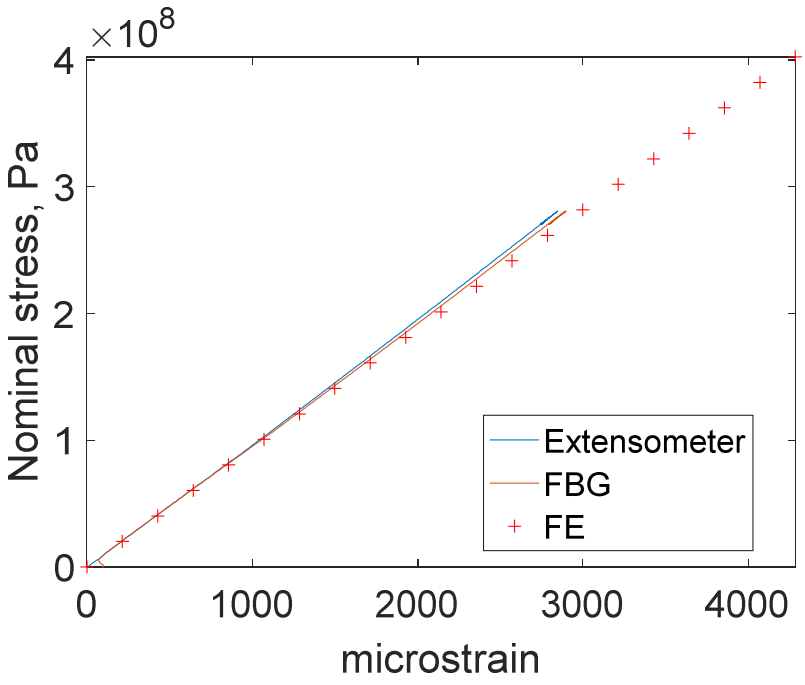

Figure 5-7: Uniaxial tensile test of composite rod with embedded FBG sensor.

Table 5.2: Elastic moduli determined from uniaxial tension.

	Elastic Modulus (GPa)
FBG	96.6
Extensometer	97.4
FE	93.9

The time-history of measured strain during a 20 kN hold in Figure 5-8 shows that the embedded FBG response follows that of the extensometer with an offset of approximately 50 με. This discrepancy in the FBG indicated strain develops as the application of load commences with a small initial compressive strain followed by an expected response to uniaxial tension. This trend is likely an artifact of initial curvature in the specimen caused by misalignment in the manufactured gripping fixtures as an initially bent specimen would exhibit compressive strain until straightened by the applied load. This phenomenon is addressed in ASTM E8 on the test method for tensile testing of metallic materials. As the load of 20 kN is reached and extension is held constant, the

maximum indicated strain values are observed, which differ by 2.1 %. For the duration of the constant extension segment, an expected viscoelastic relaxation of the PMC occurs where the indicated strains decrease by 3.5% and 3.0% for the extensometer and FBG measurements, respectively. After the viscoelastic relaxation, the extensometer and FBG measurements exhibit a difference of 1.5 %. The difference observed between the FBG and extensometer represents the micro and macro effects of viscoelastic relaxation within the composite. The included embedded FBG sensor response will be influenced by the fiber alignment and volume content of the local composite surrounding the optical fiber.

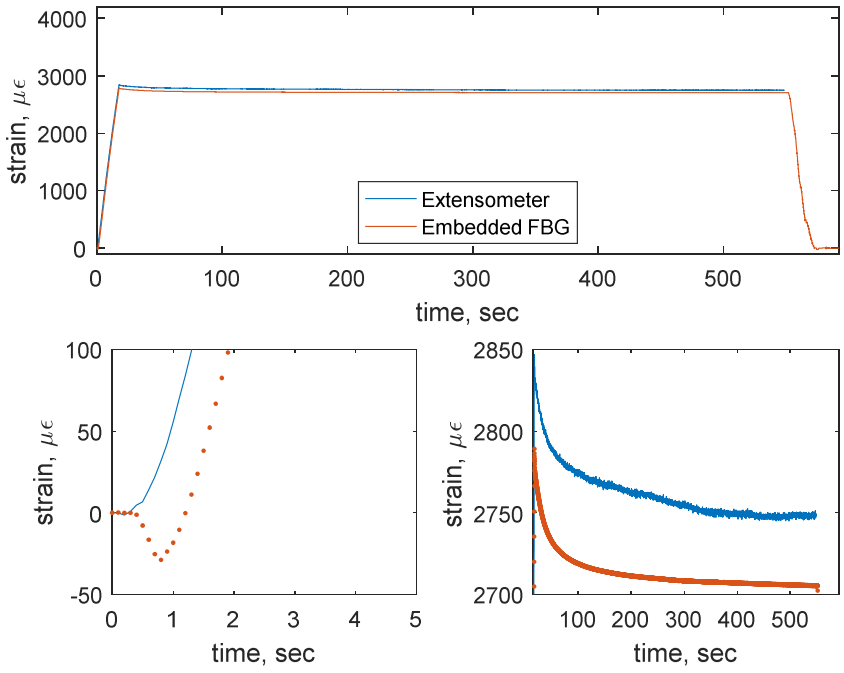

Figure 5-8: Uniaxial tension with extension hold at 20 kN.

When the maximum tensile load of the specimen is increased to 30 kN, the embedded FBG indicates a similar strain response as the external extensometer to a maximum indicated strain that differs by 1.0 % in Figure 5-9. As the extension is held constant, the extensometer indicates a constant strain after the initial expected viscoelastic creep of the

PMC, whereas the FBG indicated strain undergoes significant relaxation as time progresses and a rapid loss of strain around 400 seconds. This discrepancy at higher strain values indicates a shear failure in the interface between the optical fiber cladding and the surrounding composite.

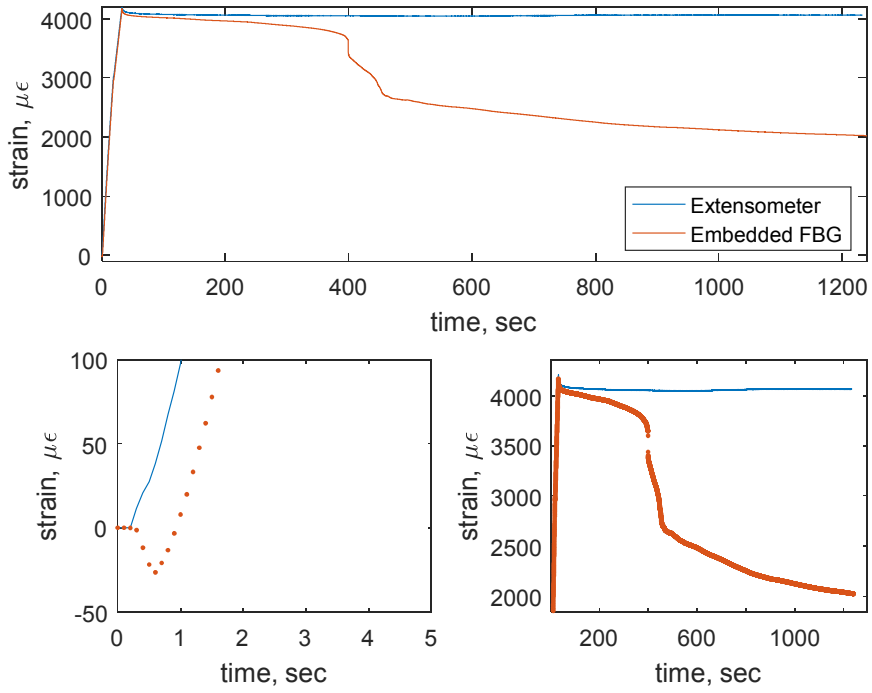

Figure 5-9: Uniaxial tension with extension hold at 30 kN.

The tensile load of 20 kN is representative of the axial loads experienced during installation, and the embedded FBG sensor successfully indicated the internal strain under this condition. The 30 kN load which approaches the typical axial service loads of 40 kN was found to exceed the capabilities of the embedded FBG sensor in the specimen and suggests that a limiting strength exists between the composite and the optical fiber.

5.4.3 Influence of acrylate buffer on indicated strains

A transverse section of the composite rod specimen received from CTC was prepared for microscopy with a JEOL 5800LV scanning electron microscope (SEM). The SEM image in Figure 5-10 clearly shows the components of the dual acrylate coated optical fiber with the surrounding constituents of the hybrid composite rod. It is clear that the dual acrylate buffer survived pultrusion. Gaps at the interface between the acrylate buffer and the cladding of the optical fiber can be seen that extend below the polished surface of the specimen and are an artifact of specimen preparation.

The polymer buffer is intended to protect the glass fiber surface from damage during handling and is optimized for easy mechanical stripping. These attributes inhibit the transfer of axial strains from the host material to the optical fiber at higher strains and result in the discrepancy between the extensometer and FBG measured strains of the 30 kN tensile test in Figure 5-9. Similar observations of the strain transfer through the buffer have been reported by Khadka [77] and Her [76].

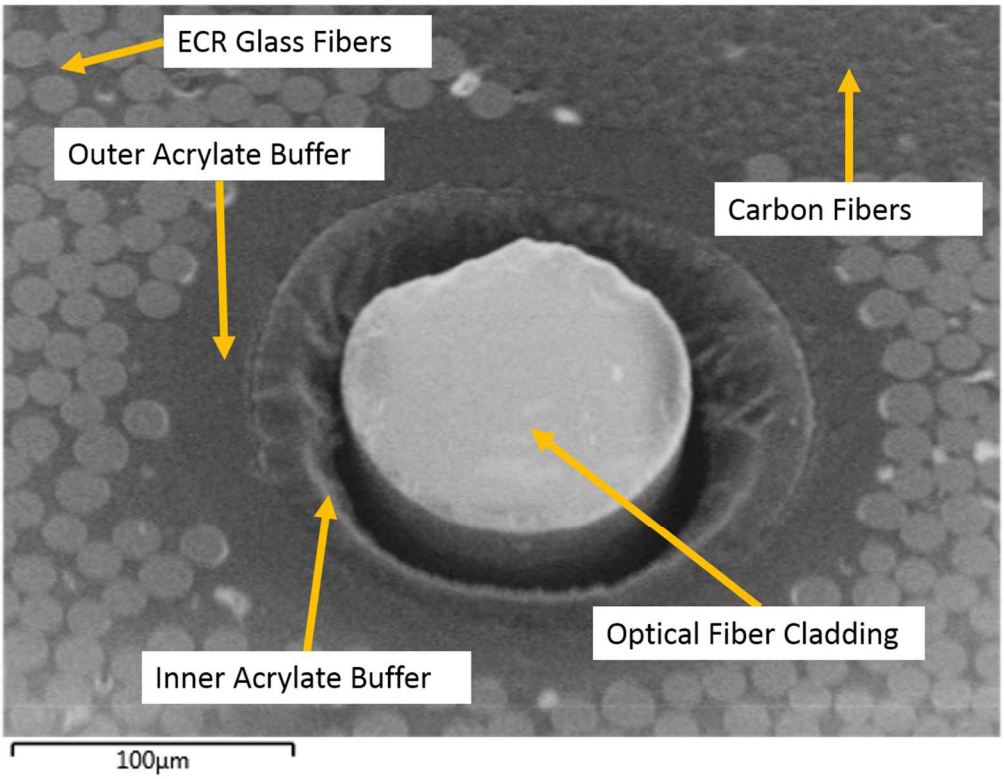

Figure 5-10: Optical fiber acrylate buffer in pultruded composite.

The interface failure of the short composite specimens utilized in this work is most similar to the pull-out conditions imposed when mechanically stripping an optical fiber. Ly, et. al identified three distinct phases in the stripping pullout failure of dual coated optical fibers and found a dependency on the length of the fiber being stripped [81]. At first, the buffer behaves linear elastically, followed by the stable initiation/propagation of a crack at the interface between the glass and the polymer buffer. Finally, after complete debonding of the glass interface, frictional sliding occurs between the glass cladding and the acrylate buffer. In the presented work, the crack most likely initiated at the transverse cut end of the composite specimens, which was only 226 mm from the edge of the gauge section in the uniaxial tension tests compared to approximately double that in the four-point test specimens.

This acrylate buffer debonding mechanism clearly influences the ability to use FBG sensors in pultruded composites as demonstrated by the results of the uniaxial tensile test in section 5.4.2. The strains induced by the 30 kN axial load appear to be above the limit for use of a dual acrylate buffered optical fiber but lower strains seem stable. Subsequent experiments are needed to evaluate the influence of sample length, and how the pultrusion processing temperature affects the strength of an acrylate buffer. Additional comparison between FBG measurements made with bare optical fiber and those with alternative buffer materials such as polyimides should be made.

5.5 Chapter conclusions

This research shows that acrylate buffered optical fibers with FBG sensors embedded in pultruded glass/carbon fiber-epoxy rods are limited to strains well below the strength of standard optical fibers and the conditions at which damage is expected in ACCC® Drake cores. Contrary to previously published work, however, the sensors can survive pultrusion and provide credible strain data from the rods subjected to either bending or axial tensile loads even with short hold times. This research also shows that if the strain transfer from the composite of a Drake size composite conductor rod, to an embedded FBG sensor is assumed perfect, a 1491 MPa (216.2kpsi) proofed SMF-28e+® fiber would provide 100% reliability anywhere in the carbon composite section of the core up to the expected damage initiating conditions. The experimental work, however, showed that a limit of the sensors' usefulness exists due to the dual acrylate buffer. In this case, the condition became apparent near the start of the 30 kN constant axial load test. After approximately 350 s, the indicated embedded strain rapidly diverged from the surface strain measured by an extensometer. The main conclusion of the work is that the sensors

can monitor strains in the rods during installation resulting from relatively low bending and tensile loads. They would not however allow the rods to be monitor for internal damage under full in service loads.

6 Concluding remarks

This work presents several important contributions that further the general understanding of the damage mechanisms in polymer core composite conductors, particularly the ACCC® conductor design. They should be of significant interest to the manufacturers and users of these conductors all over the world. This work was only possible thanks to the very generous support of two major US federal utilities, BPA and WAPA, and the main US manufacturer of the ACCC® design, CTC Global. Other industrial members of the HVT Center were also involved in this research, but to a lesser degree. The most important observations of this entire research can be summarized in the concluding remarks presented below.

It was discovered that under laboratory conditions, the low-velocity impact damage tolerance of the ACCC® conductors can be determined using a novel approach based on numerical and experimental analyses involving low-velocity impact testing with and without applied axial loads. The methodology developed here was only applied for one particular HTLS conductor design. However, it should be strongly emphasized that the methodology could also generate useful information about the resistance of other polymer composite core conductor designs to transverse impact.

For the energies tested in this research up to 33.1 J, catastrophic failure of the ACCC® was found only to occur when the conductor was not constrained by an initial

axial tension, a situation similar to that experienced during installation. This observation is important since catastrophic failures of ACCC® conductors had occurred during installation. Owing to a previously limited understanding of the conductor's mechanical response to extreme impact situations during installation, these occurrences could not be properly explained.

Overall, the most applicable situations that expose ACCC® to potential damage were identified, and a computationally efficient numerical model for static loading analysis was developed. For the boundary conditions of prescribed displacements and prescribed tensions, little difference was found in the energy dissipation and deflections of the conductors under high axial tensions. Under dynamic loading conditions, however, the simplified model provided a poor approximation of the experimental results.

The lower axial compressive strength of the carbon composite region of the composite core of the ACCC® has been hypothesized by other authors to initiate catastrophic rod collapse under pure bending conditions. The present work further supports those hypotheses and has shown numerically, analytically, and experimentally that the application of axial tension can reduce the critical bending radius which initiates damage. If the axial tension is fully controlled during installation, the probability of catastrophic bending failures will be significantly reduced.

In an ideal hybrid composite rod consisting of glass and carbon fiber regions, with the reinforcement fibers perfectly aligned, the addition of axial tension causes the micro-buckling failure mode to shift from the carbon composite region in the center to the glass region closer to the rod surface. Further increases in axial tension subsequently results in

tensile failure modes of the carbon composite region. It has been shown for the first time in this work that the presence of natural fiber misalignment in the ACCC® core significantly influences its flexural strength and must be a consideration in failure analysis. The location for the initiation of compressive damage can move away from the outermost carbon fibers (nominal location) to a region with a high degree of local misalignment. This phenomenon is most notable under pure bending, but can be mitigated with the application of axial tension. The robustness of ACCC® to bending loads would be improved if the inherent fiber misalignment were reduced. Additionally, application of axial tension can reduce the influence of misalignment and, to a point, provide more protection from bending.

With this better understanding of the failure mechanisms in ACCC® conductors and the conditions at which they can develop, the possibility for active monitoring of polymer core conductors using FBG optical fiber sensors was evaluated for the first time and then verified in the ACCC® conductor. In particular, surface adhered FBG sensors were shown to be an effective and viable sensor for monitoring ACCC® conductors and most likely other composite core conductor designs by accurately measuring strains due to static and impact loads. Static axial, bending, and combined tension-bending load cases were considered for both bare conductor rods and complete conductors with aluminum stranding. An improved finite element model provides very good agreement between the experimental FBG measured strains and their numerical predictions. Under dynamic loading scenarios, surface mounted FBG sensors were demonstrated to successfully identify and localize dynamic situations ranging from very small to large impacts.

Steady-state and transient responses of the conductor after impacts as small as 0.01 J can be detected on a 1.1 m long conductor span.

One of the most important observation made in this research is the fact that embedded FBG sensors can be used to monitor for the conditions that initiate damage in ACCC®, other polymer core composite conductor designs, and most likely other pultruded polymer matrix composites in general. Important contributions to the embedding of fiber optic FBG sensors within the pultruded composite core of ACCC® have been made. This work provides the first steps to creating a smart composite structure for use in overhead transmission lines. For a Drake sized ACCC® core, a 1491 MPa (216.2kpsi) proofed SMF-28e+® fiber would provide 100% reliability anywhere in the carbon composite section of the core up to the expected damage initiating conditions of the structure. However, dual acrylate buffered optical fibers are not recommended for embedded strain sensing in the hybrid pultruded composite of ACCC® in short lengths. At the same time, this type of fiber would be fully applicable for telecommunication purposes.

FBG optical fiber sensors are ideal for distributed sensing of a transmission line because of their form and immunity to electromagnetic fields. Sensors adhered to the surface of ACCC® cores accurately indicate the mechanical strains generated by static and dynamic loading. Furthermore, it has been demonstrated that optical fibers with FBG sensors can be embedded inside the pultruded composite core of ACCC®; however, limitations exist on the measuring capabilities because of the protective buffer. Further work is still needed to compare the indicated response of embedded optical sensors having other commercially available coatings such as single acrylate and polyimides. It

would be highly advantageous to perform the following types of testing to continue the advancement of this research:

- Comprehensive testing of the native composite strength properties for progressive failure analysis modeling.
- Impact testing at higher velocities until damage is found with CT scans.
- FBG sensor arrays with more sensors to provide more experimental data to compare with FEA results.
- Further analysis on the effect of ACCC®'s proprietary curing temperatures on the inexpensive standard dual acrylate buffer.
- Statistical evaluation of embedded optical fiber placement to quantify the theoretical uncertainty of bending calculations.
- Determination of how the composite strength is affected by embedding larger diameter optical fibers, including location, number, and diameter.

This research was performed to better characterize the conditions that can be damaging to various classes of polymer core composite conductor designs, including ACCC®. The topic was initially investigated by Burks and Kumosa [17]–[19], [21] in response to several incidents of failure. One incident in Poland where the transmission line failed suddenly three times after two years in service, and another when the conductor dropped during the installation sagging procedure in Utah. It was determined that these failures were caused by damage to the composite core from excessive bending, incurred from improper installation procedures without the level of understanding demonstrated in this research. The current work further supports their conclusion that

damage typically initiates with micro-buckling in the carbon composite from bending and additionally explains how axial tensile loading conditions influences the damage initiation mode and location in the core. With the more comprehensive fundamental understanding of the damaging conditions for ACCC®, a novel approach to monitor the structure for these conditions was then suggested and successfully verified on short laboratory ACCC® specimens.

References

[1] P. W. Parfomak, “Physical Security of the U.S. Power Grid: High-Voltage Transformer Substations Specialist in Energy and Infrastructure Policy,” R43604, Jun. 2014.

[2] “LARGE POWER TRANSFORMERS AND THE U.S. ELECTRIC GRID,” *Infrastructure Security and Energy Restoration Office of Electricity Delivery and Energy Reliability U.S. Department of Energy*, no. April. ICE Publishing, Apr-2014.

[3] F. R. Thrash, “Transmission Conductors - A Review of the Design and Selection Criteia,” *Southwire*, 2013. [Online]. Available: http://www.southwire.com/support/TransmissionConductoraReviewOfTheDesignandSelectionCriteria.htm. [Accessed: 14-Jan-2016].

[4] M. Wald, “What’s next; to avert blackouts, a sag-free cable,” *NY Times*, 2004. [Online]. Available: http://www.nytimes.com/2004/03/04/technology/what-snext-to-avert-blackouts-a-sag-free-cable.html?_rD0. [Accessed: 14-Jan-2016].

[5] W. D. Jones, “More heat, less sag [power cable upgrades],” *IEEE Spectr.*, vol. 43, no. 6, pp. 16–18, Jun. 2006.

[6] B. Clairmont, “High-Temperture Low-Sag Conductors,” in *Transmission Research Program Colloquium*, 2008.

[7] E. Håkansson, “Galvanic Corrosion of High-Temperature Low-Sag (HTLS) High Voltage Conductors : New Materials--New Challenges,” University of Denver, 2013.

[8] A. Alawar, E. J. Bosze, and S. R. Nutt, “A composite core conductor for low sag at high temperatures,” *IEEE Trans. Power Deliv.*, vol. 20, no. 3, pp. 2193–2199, 2005.

[9] CTC Global, “Engineering Transmission Lines with High Capacity Low Sag ACCC ®Conductors,” 2011.

[10] J. Hoffman, J. Middleton, and M. Kumosa, “Effect of a surface coating on flexural performance of thermally aged hybrid glass/carbon epoxy composite rods,” *Compos. Sci. Technol.*, vol. 106, pp. 141–148, 2015.

[11] S. Agrawal, K. K. Singh, and P. K. Sarkar, “Impact damage on fibre-reinforced polymer matrix composite - A review,” *J. Compos. Mater.*, vol. 48, no. 3, pp. 317–332, 2014.

[12] W. J. J. Cantwell and J. Morton, “The impact resistance of composite materials — a review,” *Composites*, vol. 22, no. 5, pp. 347–362, 1991.

[13] W. J. Cantwell and J. Morton, “Comparison of the low and high velocity impact response of CFRP,” *Composites*, vol. 20, no. 6, pp. 545–551, 1989.

[14] W. CANTWELL and J. MORTON, “THE SIGNIFICANCE OF DAMAGE AND DEFECTS AND THEIR DETECTION IN COMPOSITE-MATERIALS - A REVIEW,” *J. STRAIN Anal. Eng. Des.*, vol. 27, no. 1, pp. 29–42, 1992.

[15] Z. Y. Zhang and M. O. W. Richardson, “Low velocity impact induced damage evaluation and its effect on the residual flexural properties of pultruded GRP composites,” *Compos. Struct.*, vol. 81, pp. 195–201, 2007.

[16] C. Poon, T. Benak, and R. Gould, “Assessment of impact damage in toughened

resin composites," *Theor. Appl. Fract. Mech.*, vol. 13, no. 2, pp. 81–97, May 1990.

[17] B. M. Burks, D. L. Armentrout, M. Baldwin, J. Buckley, and M. Kumosa, "Hybrid composite rods subjected to excessive bending loads," *Compos. Sci. Technol.*, vol. 69, no. 15–16, pp. 2625–2632, 2009.

[18] B. Burks, J. Middleton, D. Armentrout, and M. Kumosa, "Effect of excessive bending on residual tensile strength of hybrid composite rods," *Compos. Sci. Technol.*, vol. 70, no. 10, pp. 1490–1496, 2010.

[19] B. Burks, D. Armentrout, and M. Kumosa, "Failure prediction analysis of an ACCC conductor subjected to thermal and mechanical stresses," *IEEE Trans. Dielectr. Electr. Insul.*, vol. 17, no. c, pp. 588–596, 2010.

[20] B. Burks, D. Armentrout, and M. Kumosa, "Characterization of the fatigue properties of a hybrid composite utilized in high voltage electric transmission," *Compos. Part A Appl. Sci. Manuf.*, vol. 42, no. 9, pp. 1138–1147, 2011.

[21] B. Burks, J. Middleton, and M. Kumosa, "Micromechanics modeling of fatigue failure mechanisms in a hybrid polymer matrix composite," *Compos. Sci. Technol.*, vol. 72, no. 15, pp. 1863–1869, 2012.

[22] F. Bowden and D. Tabor, *The friction and lubrication of solids*. Oxford : Clarendon Press, 1954.

[23] J. D. Eshelby, "The Determination of the Elastic Field of an Ellipsoidal Inclusion, and Related Problems," *Proc. R. Soc. London Ser. A-Mathmatical Phys. Sci.*, vol. 241, no. 1226, pp. 376–396, 1957.

[24] C. Dong and I. J. Davies, "Optimal design for the flexural behaviour of glass and

carbon fibre reinforced polymer hybrid composites," *Mater. Des.*, vol. 37, pp. 450–457, 2012.

[25] C. Dong, H. A. Ranaweera-Jayawardena, and I. J. Davies, "Flexural properties of hybrid composites reinforced by S-2 glass and T700S carbon fibres," *Compos. Part B Eng.*, vol. 43, no. 2, pp. 573–581, 2012.

[26] C. Dong, Sudarisman, and I. J. Davies, "Flexural properties of e glass and TR50S carbon fiber reinforced epoxy hybrid composites," *J. Mater. Eng. Perform.*, vol. 22, no. 1, pp. 41–49, 2013.

[27] C. Dong, "Uncertainties in flexural strength of carbon/glass fibre reinforced hybrid epoxy composites," *Compos. Part B Eng.*, vol. 98, pp. 176–181, 2016.

[28] P. J. Hine, M. Bonner, I. M. Ward, Y. Swolfs, I. Verpoest, and A. Mierzwa, "Hybrid carbon fibre/nylon 12 single polymer composites," *Compos. Part A Appl. Sci. Manuf.*, vol. 65, pp. 19–26, 2014.

[29] B. Burks and M. Kumosa, "The effects of atmospheric aging on a hybrid polymer matrix composite," *Compos. Sci. Technol.*, vol. 72, no. 15, pp. 1803–1811, 2012.

[30] D. H. Waters, J. Hoffman, E. Hakansson, and M. Kumosa, "Low-velocity impact to transmission line conductors," *Int. J. Impact Eng.*, vol. 106, pp. 64–72, 2017.

[31] D. H. Waters, J. Hoffman, and M. Kumosa, "Monitoring of Overhead Transmission Conductors Subjected to Static and Impact Loads Using Fiber Bragg Grating Sensors," *IEEE Trans. Instrum. Meas.*, vol. 68, no. 2, pp. 595–605, 2019.

[32] Y. Wang, Y. Chai, C. Soutis, and P. J. Withers, "Evolution of kink bands in a notched unidirectional carbon fi bre-epoxy composite under four-point bending,"

Compos. Sci. Technol., vol. 172, no. September 2018, pp. 143–152, 2019.

[33] M. R. Wisnom, "Analysis of Shear Instability in Compression Due to Fibre Waviness," *J. Reinf. Plast. Compos.*, vol. 12, no. 11, pp. 1171–1189, 1993.

[34] M. R. Wisnom, "The Effect of Fibre Waviness on the Relationship between Compressive and Flexural Strengths of Unidirectional Composites," *J. Compos. Mater.*, vol. 28, no. 1, pp. 66–76, 1994.

[35] B. Budiansky and N. A. Fleck, "Compressive failure of fibre composites," *J. Mech. Phys. Solids*, vol. 41, no. 1, pp. 183–211, 1993.

[36] N. A. Fleck, *Compressive Failure of Fiber Composites*, vol. 33, no. C. Elsevier Masson SAS, 1997.

[37] S. Lee and A. M. Waas, "Compressive response and failure of fiber reinforced unidirectional composites," *Int. J. Fract.*, vol. 100, pp. 275–306, 1999.

[38] M. R. Wisnom, "The effect of fibre misalignment on the compressive strength of unidirectional carbon fibre/epoxy," *Composites*, vol. 21, no. 5, pp. 403–407, 1990.

[39] H. M. Hsiao and I. M. Daniel, "Effect of fiber waviness on stiffness and strength reduction of unidirectional composites under compressive loading," *Compos. Sci. Technol.*, vol. 56, no. 5, pp. 581–593, 1996.

[40] T. Yokozeki, H. Takemura, and T. Aoki, "Numerical analysis on the flexural strength of unidirectional CFRTP composites with in-plane fiber bundle waviness," *Adv. Compos. Mater.*, vol. 29, no. 1, pp. 89–100, 2020.

[41] W. H. m. Van Dreumel and J. L. m. Kamp, "Non Hookean Behaviour in the Fibre Direction of Carbon-Fibre Composites and the Influence of Fibre Waviness on the

Tensile Properties," *J. Compos. Mater.*, vol. 11, no. 4, pp. 461–469, 1977.

[42] T. Yokozeki, T. Ogasawara, and T. Ishikawa, "Effects of fiber nonlinear properties on the compressive strength prediction of unidirectional carbon-fiber composites," *Compos. Sci. Technol.*, vol. 65, no. 14, pp. 2140–2147, 2005.

[43] D. Hull and T. W. Clyne, *An Introduction to Composite Materials*, 2nd ed. Cambridge University Press, 1996.

[44] J. Middleton, B. Burks, T. Wells, A. M. Setters, I. Jasiuk, and M. Kumosa, "The effect of ozone and high temperature on polymer degradation in polymer core composite conductors," *Polym. Degrad. Stab.*, vol. 98, no. 11, pp. 2282–2290, 2013.

[45] N. K. Kar, E. Barjasteh, Y. Hu, and S. R. Nutt, "Bending fatigue of hybrid composite rods," *Compos. Part A Appl. Sci. Manuf.*, vol. 42, no. 3, pp. 328–336, 2011.

[46] J. Middleton, J. Hoffman, B. Burks, P. Predecki, and M. Kumosa, "Aging of a polymer core composite conductor: Mechanical properties and residual stresses," *Compos. Part A Appl. Sci. Manuf.*, vol. 69, pp. 159–167, 2015.

[47] P. Rupnowski, M. Gentz, J. K. Sutter, and M. Kumosa, "An evaluation of the elastic properties and thermal expansion coefficients of medium and high modulus graphite fibers," *Compos. Part A Appl. Sci. Manuf.*, vol. 36, no. 3, pp. 327–338, 2005.

[48] D. Mounier, C. Poilane, C. Bucher, and P. Picart, "Evaluation of transverse elastic properties of fibers used in composite materials by laser resonant ultrasound

spectroscopy," *Proc. Acoust. 2012 Nantes Conf.*, no. April, pp. 1247–1250, 2012.

[49] Toray, "Carbon Fiber T700S," p. 2, 2018.

[50] "Standard Test Method for Flexural Properties of Unreinforced and Reinforced Plastics and Electrical Insulating Materials by Four-Point Bending 1," *Annu. B. ASTM Stand.*, vol. 08, no. June, pp. 1–8, 2010.

[51] CTC Global, "ACCC Drake datasheet," 2019.

[52] K. H. Lo and E. S. Chim, "Compressive Strength of Unidirectional Composites," *J. Reinf. Plast. Compos.*, vol. ll, no. August, pp. 838–896, 1992.

[53] U. Breiman, J. Aboudi, and R. Haj-Ali, "Semianalytical compressive strength criteria for unidirectional composites," *J. Reinf. Plast. Compos.*, vol. 37, no. 4, pp. 238–246, 2018.

[54] M. R. Wisnom, "On the high compressive strains achieved in bending tests on unidirectional carbon-fibre/epoxy," *Compos. Sci. Technol.*, vol. 43, no. 3, pp. 229–235, 1992.

[55] D. B. Miracle and S. L. Donaldson, Eds., "Composites," vol. 21, no. Ref 19. ASM International, 01-Jan-2001.

[56] B. Budiansky, N. A. Fleck, and J. C. Amazigo, "On kink-band propagation in fiber composites," *J. Mech. Phys. Solids*, vol. 46, no. 9, pp. 1637–1653, 1998.

[57] E. Hakansson, P. Predecki, and M. S. Kumosa, "Galvanic Corrosion of High Temperature Low Sag Aluminum Conductor Composite Core and Conventional Aluminum Conductor Steel Reinforced Overhead High Voltage Conductors," *IEEE Trans. Reliab.*, vol. 64, no. 3, pp. 928–934, 2015.

[58] J. Middleton, B. Burks, T. Wells, A. M. Setters, I. Jasiuk, and M. Kumosa, "The effect of ozone on polymer degradation in polymer core composite conductors," *Polym. Degrad. Stab.*, vol. 98, no. 11, pp. 2282–2290, 2013.

[59] R. Kashyap, "Principles of Optical Fiber Grating Sensors," *Fiber Bragg Gratings*, pp. 441–502, 2010.

[60] K. O. Hill and G. Meltz, "Fiber Bragg Grating Technology Fundementals and Overview," *IEEE J. Light. Technol.*, vol. 15, no. 8, pp. 1263–1276, 1997.

[61] "FIBER BRAGG GRATING (FBG) SENSOR PRINCIPLE." [Online]. Available: http://www.fbgs.com/technology/fbg-principle/. [Accessed: 15-Dec-2017].

[62] M. Zhang, Y. Xing, Z. Zhang, and Q. Chen, "Design and experiment of FBG-based icing monitoring on overhead transmission lines with an improvement trial for windy weather," *Sensors (Switzerland)*, vol. 14, no. 12, pp. 23954–23969, 2014.

[63] G.-M. Ma, C.-R. Li, J. Jiang, J.-Y. Liang, Y.-T. Luo, and Y.-C. Cheng, "A Passive Optical Fiber Anemometer for Wind Speed Measurement on High-Voltage Overhead Transmission Lines," *IEEE Trans. Instrum. Meas.*, vol. 61, no. 2, pp. 539–544, 2012.

[64] G. Ma, N. Mao, Y. Li, J. Jiang, H. Zhou, and C. Li, "The Reusable Load Cell with Protection Applied for Online Monitoring of Overhead Transmission Lines Based on Fiber Bragg Grating," *Sensors*, vol. 16, no. 6, p. 922, 2016.

[65] J. Luo, Y. Y. Hao, Q. Ye, Y. Y. Hao, and L. Li, "Development of optical fiber sensors based on brillouin scattering and FBG for on-line monitoring in overhead

transmission lines," *J. Light. Technol.*, vol. 31, no. 10, pp. 1559–1565, 2013.

[66] G. ming Ma *et al.*, "A novel optical load cell used in icing monitoring on overhead transmission lines," *Cold Reg. Sci. Technol.*, vol. 71, pp. 67–72, Feb. 2012.

[67] G. M. Ma, C. R. Li, J. T. Quan, J. Jiang, and Y. C. Cheng, "A fiber bragg grating tension and tilt sensor applied to icing monitoring on overhead transmission lines," *IEEE Trans. Power Deliv.*, vol. 26, no. 4, pp. 2163–2170, 2011.

[68] L. Bjerkan, "Application of fiber-optic bragg grating sensors in monitoring environmental loads of overhead power transmission lines.," *Appl. Opt.*, vol. 39, no. 4, pp. 554–560, 2000.

[69] J. Hoffman, D. H. Waters, S. Khadka, and M. S. Kumosa, "Shape Sensing of Polymer Core Composite Electrical Transmission Lines Using FBG Sensors," *IEEE Trans. Instrum. Meas.*, vol. PP, pp. 1–9, 2019.

[70] A. L. Kalamkarov, S. B. Fitzgerald, D. O. MacDonald, and A. V. Georgiades, "Processing and characterization of smart composite reinforcement," *Smart Struct. Mater. 1998 Smart Mater. Technol.*, vol. 3324, no. July 1998, p. 290, 1998.

[71] A. L. Kalamkarov, D. O. MacDonald, S. B. Fitzgerald, and A. V Georgiades, "Reliability assessment of pultruded FRP reinforcements with embedded fiber optic sensors," *Compos. Struct.*, vol. 50, no. 1, pp. 69–78, 2000.

[72] A. L. Kalamkarov, S. B. Fitzgerald, and D. O. MacDonald, "Use of Fabry Perot fiber optic sensors to monitor residual strains during pultrusion of FRP composites," *Compos. Part B Eng.*, vol. 30, no. 2, pp. 167–175, 1999.

[73] A. L. Kalamkarov, H. Q. Liu, and D. O. MacDonald, "Experimental and analytical

studies of smart composite reinforcement," *Compos. Part B Eng.*, vol. 29, no. 1, pp. 21–30, 1998.

[74] A. L. Kalamkarov, D. O. MacDonald, and P. A. D. Westhaver, "Pultrusion of smart FRP composites," in *Smart Structures and Materials 1997: Smart Sensing, Processing, and Instrumentation*, 1997, vol. 3042, no. June 1997, pp. 400–409.

[75] A. L. Kalamkarov, S. B. Fitzgerald, D. O. MacDonald, and A. V. Georgiades, "On the processing and evaluation of pultruded smart composites," *Compos. Part B Eng.*, vol. 30, no. 7, pp. 753–763, 1999.

[76] S. C. Her and C. Y. Huang, "Effect of coating on the strain transfer of optical fiber sensors," *Sensors*, vol. 11, no. 7, pp. 6926–6941, 2011.

[77] S. Khadka, J. Hoffman, and M. Kumosa, "FBG monitoring of curing in single fiber polymer composites," *Compos. Sci. Technol.*, vol. 198, no. June, p. 108308, 2020.

[78] D. Waters, J. Hoffman, and M. Kumosa, "Effect of fiber misalignment on bending strength of pultruded hybrid polymer matrix composite rods subjected to bending and tension," *Compos. Part A Appl. Sci. Manuf.*, vol. 143, no. October 2020, p. 106287, Apr. 2021.

[79] W. Griffioen and G. S. Glaesemann, "Optical fiber mechanical reliability: Review of Research at Corning's Optical Fiber Strength Laboratory White Paper," *Corning*, no. July. p. 209, 2017.

[80] CTC Global, "Engineering Transmission Lines with High Capacity Low Sag ACCC ® Conductors," 2011.

[81] H. Ly, M. Tabaddor, C. Aloisio, K. Konstadinidis, T. Goddard, and K. I. Jacob, "Coating failure in the pull-out of a multiply-coated optical fiber," *Polym. Test.*, vol. 24, no. 8, pp. 953–962, 2005.

Appendix

Figure 3-4 shows the stresses across the composite rod at four different tensions when formed around one curvature. The finite element model was subjected to four separate analyses, one for each of the tensions. This was done for six different curvatures and the results show the maximum stresses at the four locations where failure is expected to occur (glass tensile and compressive surfaces, along with the carbon tensile and compressive locations at the interface). The analytical curves presented were calculated by applying equation 3.5.

In Figure 3-5, the analytical curves presented were calculated using equation 3.6 to show the combination of load and curvature that produce the failure initiating stresses according to sec 3.3.1. For the numerical curves in Figure 3-5, the finite elements model was run with all combinations of four axial tensions and six curvatures. Using MATLAB, a first order surface was fit to the axial stress results at each of the four locations where failure is expected to occur (glass tensile and compressive surfaces, along with the carbon tensile and compressive locations at the interface). This surface fitting approach creates a numerical expression of the axial stress at each of the four locations where damage is expected to initiate, and allows for the interpolation and extrapolation of axial stress as a function of applied load and curvature. Surface regressions of higher order were evaluated, but not found to improve the fit.